Gradient enhanced multi-scale modeling framework for glass fiber reinforced polyamides

Soheil Satouri, George Chatzigeorgiou, Adil Benaarbia, Fodil Meraghni

Gradient enhanced multi-scale modeling framework for glass fiber reinforced polyamides

Soheil Satouri, George Chatzigeorgiou, Adil Benaarbia, Fodil Meraghni*

Arts et Métiers Institute of Technology, CNRS, Université de Lorraine, LEM3, F-57000, Metz, France

Abstract

This study proposes a multi-scale gradient enhanced nonlocal modeling framework aimed at predicting the mechanical response of long glass fiber reinforced polyamide composites that exhibit nonlinear viscoelastic viscoplastic rheology with ductile damage driven by plasticity. To treat numerically material instabilities at severe damage levels, an internal length scale is introduced within the model through a gradient enhanced framework that controls the non-physical localization of state variables and the consequent early model failures. To do so, a viscoelastic viscoplastic phenomenological model is adopted to capture the matrix phase nonlinear response at the microscale, then an appropriate homogenization approach is adopted to provide the overall response of the composite, in which the gradient enhanced framework is imposed at the macroscale. As a result, a consistent homogenization model capable of capturing nonlocal phenomena is introduced and implemented in a commercial finite element software, which addresses the non-physical responses of the local model and exhibits higher stability.

Keywords: gradient enhanced modeling, homogenization techniques, finite element simulations, polyamide composites.

1. Introduction

Polyamide-based composites are among the most widely used materials in a variety of industries like aerospace, automotive, and energy thanks to their advantages such as durability, multifunctionality, and strength. Accordingly, engineers need to have a more accurate understanding on

*Corresponding author
Email address: fodil.meraghni@ensam.eu (Fodil Meraghni)

their mechanical behavior under loading, particularly when exceeding the elastic limits and experiencing damage or the consequent failure. Matrix phase consisting of polyamide exhibits inelastic mechanisms along with ductile damage driven by plasticity. To model the nonlinear mechanisms of the polymer phase, many constitutive models have been proposed in the literature (Boyce et al., 1988; Arruda & Boyce, 1993; Buckley & Jones, 1995; Tervoort et al., 1997; Govaert et al., 2000; Klompen et al., 2005). However, to investigate the global mechanical behavior of composite structures, it is necessary to model them as homogeneous materials based on multi-scale homogenization theories (Castañeda, 1991; Terada & Kikuchi, 2001; Meraghni et al., 2002; Love & Batra, 2006; Suquet, 2012; Mareau et al., 2012; Fritzen et al., 2012; Wu et al., 2013; Chatzigeorgiou et al., 2016; Praud et al., 2017b; Tikarrouchine et al., 2018; Kotha et al., 2019; Chatzigeorgiou et al., 2019, 2020; Praud et al., 2021a; Tikarrouchine et al., 2021).

In our previous studies, to model nonlinear inelastic mechanical responses of pure polymers, the VEVPD model has been developed (Praud et al., 2017a), based on which several multi-scale models have also been presented to predict the behavior of composites through full-field finite element-based and mean-field approaches (Tikarrouchine et al., 2021; Chen et al., 2021). However, the latter frameworks provide reliable responses for relatively low damage levels. To address this issue, initially, the non-physical responses at high damage levels in the pure matrix have been addressed by developing a nonlocal gradient enhanced model (Satouri et al., 2022). The present study considers the latter nonlocal model and develops a multi-scale framework capable of capturing the behavior of composites at high levels of damage.

It should be pointed out that the gradient enhancement in terms of damage or hardening has been extensively discussed in the previous work by the authors (Satouri et al., 2022), as well as in Dimitrijevic & Hackl (2011). For the sake of completeness, the drawn conclusions justifying the interest of nonlocal hardening versus the nonlocal damage are summarized as follows: (i) Investigation of the numerical examples demonstrated that the nonlocal variable based on the viscoplastic hardening (r^{nl}) is more suitable to control the damage localization. (ii) The approach based on the nonlocal damage variable (D^{nl}) was shown to be unable to represent the damage localization, while a spurious plasticity localization appears during the material softening. (iii) From the model formulation, it is evident that viscoplasticity drives damage and their evolutions are directly related by complementary laws, but the reverse does not occur.

Multi-scale homogenization framework addresses the composite behavior at both the macro and

micro scales. It considers the mechanisms of the composite constituents as well as their geometry characteristics and configurations in the microstructure, based on which the overall mechanical behavior of the composite are interpreted as a homogeneous material at the macroscale. In this connection, many finite element based homogenization and mean field approaches are proposed in the literature. From a technical prospect, mean field models are computationally less expensive than finite element-based approaches, which has made their application more popular. The Mori-Tanaka approach is among the most widely used of them, which was first applied to elastic models for estimating the average stress in materials with inclusions (Mori & Tanaka, 1973), and then extended to investigate nonlinear inelastic mechanisms (Remond, 2005; Aboudi, 2005; Mahnken et al., 2009; Paquet et al., 2011; Mareau et al., 2012). Many researchers extended this framework to also obtain the global stiffness using the material properties of the constituents (Benveniste, 1987; Lagoudas et al., 1991; Desrumaux et al., 2001). For nonlinear materials, Transformation Field Analysis (TFA) allows estimating the overall behavior of the composite when the matrix phase exhibits inelastic mechanisms (Dvorak & Benveniste, 1992; Kruch & Chaboche, 2011; Chatzigeorgiou & Meraghni, 2019). However, some shortcomings have been reported in the literature regarding the classical model, related to stiff predicted response due to inability to capture properly the inelastic strains, especially in the matrix phase. To resolve this issue, several techniques have been proposed in the literature, among them the isotropization technique (Doghri & Ouaar, 2003), a method involving the Linear Comparison Composite (Lahellec & Suquet, 2007) and an approach considering a coating layer with increased inelastic strains (Barral et al., 2020; Chen et al., 2021). However, typical multi-scale models are inappropriate to provide accurate results at high damage levels; numerical instabilities in small zones appear as non-physical elevated stress values leading to early numerical model failure. To this end, nonlocal approaches are proposed to capture the mechanical behavior of reinforced polymer composites exhibiting high damage level even at moderate strains (less than 10%).

Conventional local models consider state variables locally, which leads to non-unique and non-physical responses in computational models when considering severely damaged structures. However, the nonlocal frameworks suggest that the values of the state variables are affected by their neighborhood weighted average. The nonlocal approach, in its classical integral form, introduces the nonlocal variable as the weighted integral of the considered local state variable over the body volume. The latter approach has been used to study the nonlinear mechanical behavior of metals

and polymers (Pijaudier-Cabot & Bažant, 1987; Jirásek et al., 1998; Jirásek, 2002; Jirásek et al., 2004; Brunet et al., 2005; Shutov & Klyuchantsev, 2021). The nonlocal integral-form formulation can be reduced to the gradient ones, in which a new degree of freedom, as the nonlocal variable, is added to the system, and an additional equation must be satisfied in conjunction with the stress equilibrium. The gradient models are more easily finite element implementable compared to the integral-form formulation (Bažant et al., 1984; Peerlings et al., 2001; Jirásek, 2007; Forest, 2009; Dimitrijevic & Hackl, 2011). Furthermore, phase field and peridynamics are other nonlocal approaches proposed in the literature (Silling, 2000; Silling & Lehoucq, 2010; Miehe et al., 2010, 2016; Praud et al., 2021b). The nonlocal variable is generally chosen based on the dominant nonlinear mechanisms, in which non-unique and unstable responses are observed (Jirásek et al., 1998; Geers et al., 1999; Simone et al., 2004; Wu et al., 2013). The nonlocal variable can be incorporated within the model using different ways. The first consists in replacing the local variable by its nonlocal counterpart directly in the constitutive laws (Geers et al., 2000). Another way is to consider both local and nonlocal variables and combine them through Kuhn-Tucker conditions as proposed by Seupel et al. (2018). The third way is to apply an extended thermodynamical framework, in which the free energy potential is enhanced with a nonlocal part (Dimitrijevic & Hackl, 2011; Kiefer et al., 2018; Ostwald et al., 2019), as the micromorphic approach (Forest, 2009).

This work aims at investigating the mechanical behavior of a polyamide-based composite in presence of high level of ductile damage. The early model limits, leading to non-physical responses, are addressed through a nonlocal gradient enhanced approach. The relationship between the nonlocal length scale and RVE size is established, and a suitable homogenization framework is applied to properly capture the overall composite response. By taking the nonlocal variable homogeneous by phase, the Mori-Tanaka mean field homogenization framework along with transformation field analysis is adopted to explore the global behavior of the composite. The novelty of this research is the development of a multi-scale nonlocal framework which captures mechanisms such as viscoelasticity, viscoplasticity and ductile damage for the matrix phase, providing more stable results compared to the local framework.

This paper is structured as follows: in section 2, the theoretical framework is presented. First, the nonlinear inelastic behavior of the matrix phase and the corresponding constitutive laws are discussed, and then an appropriate multi-scale scheme is introduced, based on which the Mori-Tanaka/TFA homogenization framework is applied and formulated. In section 3, the model is first

validated with a multi-layered structure, then the application of the framework is justified with a numerical example, and finally, several examples are investigated as parametric studies.

2. Theoretical modeling framework

2.1. Matrix phase material modeling

2.1.1. Nonlinear behavior of the matrix phase

Experimental observations in the literature show that the investigated polyamide (i.e. semi-crystalline polyamide 66) exhibits nonlinear and dissipative mechanisms such as viscoelasticity at different time scales (short, medium, long and very-long term viscoelasticities), viscoplasticity, and ductile damage (Arif et al., 2014a; Benaarbia et al., 2014, 2016; Praud et al., 2017a; Benaarbia et al., 2019). Such nonlinear rheological behavior can be captured either by macro-molecular network-based or phenomenological approaches (Arruda & Boyce, 1993; Launay et al., 2011; Billon, 2012; Krairi & Doghri, 2014), derived from Thermodynamics of Irreversible Processes (TIP) coupled with Generalised Standard Materials formalism (Halphen & Nguyen, 1975; Germain et al., 1983). In the present work, a Viscoelastic Viscoplastic model with ductile Damage (VEVPD) is proposed to describe the nonlinear behavior of the polyamide matrix. The viscoplasticity is activated once the model surpasses the von Mises yield function, such that:

$$f(\boldsymbol{\sigma}, -R; D, r) = \frac{\sigma^{eq}(\boldsymbol{\sigma})}{1-D} - R(r) - R_0, \tag{1}$$

where $\boldsymbol{\sigma}$, R, R_0 and r are the second order stress tensor, the conjugate hardening state variable, the elastic limit, and the hardening state variable, respectively, while σ^{eq} denotes the equivalent stress obtained through $\sqrt{\frac{3}{2}\boldsymbol{\sigma}' : \boldsymbol{\sigma}'}$, in which $\boldsymbol{\sigma}'$ is the deviatoric part of the stress tensor, and " : " symbol denotes the double contracted product. The material degradation is considered through the scalar damage variable, D ($0 \leq D \leq 1$), based on the effective stress tensor concept (i.e. $\boldsymbol{\sigma}_{eff} = \frac{\boldsymbol{\sigma}}{1-D}$). A power-law like function for the hardening state variable rate is adopted:

$$\dot{r} = \langle \frac{f(\boldsymbol{\sigma}, -R; D, r)}{R_{vp}} \rangle_{+}^{p_{vp}^{-1}}, \tag{2}$$

where "$\langle\,.\,\rangle_{+}$" stands for the Macauley bracket, and R_{vp} and p_{vp} respectively denote the viscoplastic resistance and exponent. In this study, a Kelvin-Voigt viscoelastic model along with the unified viscoplasticity theory considering the isotropic hardening function is adopted to capture the inelastic

mechanisms of the matrix phase. In the present work, the damage is considered ductile which is driven through viscoplasticity, and the damage evolution is directly related to the hardening state variable rate, $\dot{r}$. The theoretical framework of the phenomenological model and the corresponding thermodynamic state and evolution laws are detailed in Praud et al. (2017a).

2.1.2. Thermodynamically-based Euler-Lagrange equations for the matrix phase

Since, local typical continuum models do not yield unique and physical responses in high levels of damage due to material instability, a gradient enhanced nonlocal approach is adopted to model the material behavior more precisely. To this end, the nonlocal variable is introduced to the model whose quantity depends on the spatial average of the corresponding neighborhood. The neighborhood size is determined by the internal length scale, l^{nl}. In the forthcoming sections, instead of using length scale nonlocal parameters, ξ^{nl} and γ^{nl} are used which are linked to each other through the formula: $l^{nl} = \sqrt{\xi^{nl}/\gamma^{nl}}$. To derive the Euler-Lagrange equations, the thermodynamic potential is split into two parts: local, Ψ^l and nonlocal, Ψ^{nl}:

$$\Psi\left(\boldsymbol{\epsilon}, \{\chi_i\}_{i=1,N}, r^{nl}, \boldsymbol{\nabla}_x r^{nl}\right) = \Psi^l\left(\boldsymbol{\epsilon}, \{\chi_i\}_{i=1,N}\right) + \Psi^{nl}(r, r^{nl}, \boldsymbol{\nabla}_x r^{nl}), \tag{3}$$

where $\boldsymbol{\epsilon}$ is the second-order strain tensor, and the internal state variables are summarized by $\{\chi_i\}_{i=1,N}$ which contains the hardening state variable, r, the damage, D, the viscoelastic strain tensors, $\{\boldsymbol{\epsilon}^{vi}\}_{i=1,N_v}$, and the viscoplastic strain tensor, $\boldsymbol{\epsilon}^{vp}$. Here, r^{nl} is the nonlocal counterpart of the hardening state variable, and $\boldsymbol{\nabla}_x r^{nl}$ denotes its spatial gradient. The local thermodynamic potential, Ψ^l, can be divided into three parts: the elastic part, Ψ^e, the set of viscoelastic potentials, $\{\Psi^{vi}\}_{i=1,N_v}$, and the viscoplastic free energy, Ψ^{vp}:

$$\Psi^l\left(\boldsymbol{\epsilon}, \{\boldsymbol{\epsilon}^{vi}\}_{i=1,N_v}, \boldsymbol{\epsilon}^{vp}, r, D\right) = \Psi^e\left(\boldsymbol{\epsilon}, \boldsymbol{\epsilon}^{vp}, \{\boldsymbol{\epsilon}^{vi}\}_{i=1,N_v}, D\right) + \sum_{i=1}^{N_v} \Psi^{vi}\left(\{\boldsymbol{\epsilon}^{vi}\}_{i=1,N_v}, D\right) + \Psi^{vp}(r), \tag{4}$$

with (Praud et al., 2017a)

$$\Psi^e(\boldsymbol{\epsilon}, \boldsymbol{\epsilon}^{vi}, \boldsymbol{\epsilon}^{vp}, D) = \frac{1}{2}\left(\boldsymbol{\epsilon} - \sum_{i=1}^{N_v} \boldsymbol{\epsilon}^{vi} - \boldsymbol{\epsilon}^{vp}\right) : (1-D)\mathbb{C}^e : \left(\boldsymbol{\epsilon} - \sum_{i=1}^{N_v} \boldsymbol{\epsilon}^{vi} - \boldsymbol{\epsilon}^{vp}\right), \tag{5a}$$

$$\Psi^{vi}(\boldsymbol{\epsilon}^{vi}, D) = \frac{1}{2}\boldsymbol{\epsilon}^{vi} : (1-D)\mathbb{C}^{vi} : \boldsymbol{\epsilon}^{vi}, \qquad \text{for } i = 1, ..., N_v, \tag{5b}$$

$$\Psi^{vp}(r) = \int_0^r R(\alpha) d\alpha, \tag{5c}$$

where $\mathbb{C}^e$ is the fourth order elastic stiffness tensor, and $\mathbb{C}^{vi}$ is the fourth order stiffness tensor of the corresponding Kelvin-Voigt viscoelastic branch. The nonlocal potential is proposed by Forest (2009) and defined as:

$$\Psi^{nl}(r, r^{nl}, \boldsymbol{\nabla}_x r^{nl}) = \frac{\xi^{nl}}{2} \left\| \boldsymbol{\nabla}_x r^{nl} \right\|^2 + \frac{1}{2} \gamma^{nl} (r - r^{nl})^2, \tag{6}$$

where $\|.\|$ denotes the Frobenius norm, and ξ^{nl} and γ^{nl} are the nonlocal parameters defining the neighborhood size in the nonlocal model, in which ξ^{nl} determines the degree of nonlocal regularization in the nonlocal portion of the free energy, and γ^{nl} identifies the level of interaction between the nonlocal and local variables. In other words, a proper value of γ^{nl} ensures that the local variable behaves similarly to its nonlocal counterpart (Forest, 2009; Kiefer et al., 2018; Ostwald et al., 2019). The equilibrium equations are obtained using the minimum potential energy postulate based on the above thermodynamic potentials. To this end, the total potential energy, Π, is defined as sum of the external, $-\Pi_{ext}$, and internal potential energies, Π_{int}, over a reference domain $\mathcal{B}$:

$$\Pi = \Pi_{int} - \Pi_{ext} = \int_{\mathcal{B}} \Psi \left(\boldsymbol{\epsilon}, \{\chi_i\}_{i=1,N}, r^{nl}, \boldsymbol{\nabla}_x r^{nl} \right) \, dV - \int_{\mathcal{B}} \boldsymbol{u}.\boldsymbol{F}_b \, dV - \int_{\partial \mathcal{B}} \boldsymbol{u}.\boldsymbol{F}_s \, dS \,, \tag{7}$$

where "." is the symbol for scalar product that corresponds to the tensorial single contraction. $\boldsymbol{u}$ represents the displacement vector, and $\boldsymbol{F}_b$ and $\boldsymbol{F}_s$ denote the external forces per unit volume and area respectively. Based on the minimum total potential energy hypothesis as proposed by Kiefer et al. (2018), the following minimization problem can be defined:

$$\{\boldsymbol{u}, r^{nl}\} = \arg \left[\min_{\boldsymbol{u}, r^{nl} \in \mathcal{B}} (\Pi) \right]. \tag{8}$$

Hence, the total potential energy differential is set to zero when there is an infinitesimal variation in $\boldsymbol{u}$ or r^{nl}:

$$\frac{\partial \Pi}{\partial \boldsymbol{u}}.\delta \boldsymbol{u} = \int_{\mathcal{B}} \frac{\partial \Psi}{\partial \boldsymbol{\epsilon}} : \left(\frac{\partial \boldsymbol{\epsilon}}{\boldsymbol{u}}.\delta \boldsymbol{u} \right) \, dV - \int_{\mathcal{B}} \boldsymbol{F}_b.\delta \boldsymbol{u} \, dV - \int_{\partial \mathcal{B}} \boldsymbol{F}_s.\delta \boldsymbol{u} \, dS = 0, \tag{9a}$$

$$\frac{\partial \Pi}{\partial r^{nl}} \delta r^{nl} = \int_{\mathcal{B}} \left[\xi^{nl} \boldsymbol{\nabla}_x r^{nl}.\boldsymbol{\nabla}_x \delta r^{nl} - \gamma^{nl} \left(r - r^{nl} \right) \delta r^{nl} \right] \, dV = 0. \tag{9b}$$

Under the small deformation assumption, the strain tensor, $\boldsymbol{\epsilon}$, is derived as the symmetrical gradient of the displacement vector, $\boldsymbol{\nabla}_x^{sym}\boldsymbol{u}$, upon which and by using Gauss-Ostrogradski theorem, (9a) can be expressed as follows:

$$-\int_{\mathcal{B}}(\boldsymbol{\nabla}_x.\boldsymbol{\sigma}).\delta\boldsymbol{u}\,dV+\int_{\partial\mathcal{B}}(\boldsymbol{\sigma}.\boldsymbol{n}).\delta\boldsymbol{u}\,dV-\int_{\mathcal{B}}\boldsymbol{F}_b.\delta\boldsymbol{u}\,dV-\int_{\partial\mathcal{B}}\boldsymbol{F}_s.\delta\boldsymbol{u}\,dS=0. \tag{10}$$

Considering Gauss-Ostrogradski theorem, (9b) can be written as:

$$\int_{\partial\mathcal{B}}\xi^{nl}\boldsymbol{\nabla}_x r^{nl}\delta r^{nl}.\boldsymbol{n}\,dS-\int_{\mathcal{B}}\xi^{nl}\boldsymbol{\nabla}_x^2 r^{nl}\delta r^{nl}\,dV-\int_{\mathcal{B}}\gamma^{nl}\left(r-r^{nl}\right)\delta r^{nl}\,dV=0. \tag{11}$$

The nonlocal balance equation and the stress equilibrium with their associated boundary conditions are derived from (10) and (11):

- stress equilibrium:

$$\boldsymbol{\nabla}_x.\boldsymbol{\sigma}+\boldsymbol{F}_b=0\quad\forall\boldsymbol{x}\in\mathcal{B},\quad\boldsymbol{\sigma}.\boldsymbol{n}-\boldsymbol{F}_s=0\quad\forall\boldsymbol{x}\in\partial\mathcal{B}. \tag{12}$$

- nonlocal balance equation:

$$\xi^{nl}\boldsymbol{\nabla}_x^2 r^{nl}+\gamma^{nl}\left(r-r^{nl}\right)=0\quad\forall\boldsymbol{x}\in\mathcal{B},\quad\boldsymbol{\nabla}_x r^{nl}.\boldsymbol{n}=0\quad\forall\boldsymbol{x}\in\partial\mathcal{B}. \tag{13}$$

2.1.3. State and evolution laws for the matrix phase

Derivatives of the thermodynamic potential, Ψ, with respect to the internal state variables, $\{\chi_i\}_{i=1,N}$, yield the conjugate state variables, $\{\mathcal{A}_i\}_{i=1,N}$:

$$\mathcal{A}_i=\frac{\partial\Psi}{\partial\chi_i},\quad\text{with}\quad i=1,..,N. \tag{14}$$

Apart from the standard terms, the nonlocal equation imposes some extra terms to the state laws:

- additional nonlocal state laws:

$$Y_{r^{nl}}=\frac{\partial\Psi}{\partial r^{nl}},\quad\boldsymbol{Y}_{\boldsymbol{\nabla}_x r^{nl}}=\frac{\partial\Psi}{\partial\boldsymbol{\nabla}_x r^{nl}}. \tag{15}$$

  where $Y_{r^{nl}}$ and $\boldsymbol{Y}_{\boldsymbol{\nabla}_x r^{nl}}$ are the nonlocal conjugate state variables.

- nonlocal term into the hardening conjugate state variable:

$$R=R^l+R^{nl},\quad\text{with}\quad R^l=H_m\,r^{H_p},\quad R^{nl}=\frac{\partial\Psi^{nl}}{\partial r}=\gamma^{nl}(r-r^{nl}). \tag{16}$$

The state laws in the present model are summarized and given in detail in the table 1. The intrinsic dissipation is derived from the thermodynamic potential in the rate form:

$$\mathcal{D} = P_m - \dot{\Psi} \geq 0, \tag{17}$$

where P_m stands for sum of the strain and nonlocal energy rates given as :

$$P_m = \boldsymbol{\sigma} : \dot{\boldsymbol{\epsilon}} + Y_{r^{nl}} \dot{r}^{nl} + \boldsymbol{Y}_{\boldsymbol{\nabla}_x r^{nl}} . (\boldsymbol{\nabla}_x \dot{r}^{nl}). \tag{18}$$

Considering the state laws given in the table 1, the dissipation, $\mathcal{D}$, is expanded as:

$$\begin{aligned} \mathcal{D} = {} & \boldsymbol{\sigma} : \dot{\boldsymbol{\epsilon}} + Y_{r^{nl}} \dot{r}^{nl} + \boldsymbol{Y}_{\boldsymbol{\nabla}_x r^{nl}} . (\boldsymbol{\nabla}_x \dot{r}^{nl}) \\ & - \left(\frac{\partial \Psi}{\partial \boldsymbol{\epsilon}} : \dot{\boldsymbol{\epsilon}} + \frac{\partial \Psi}{\partial \boldsymbol{\epsilon}^{vp}} : \dot{\boldsymbol{\epsilon}}^{vp} + \sum_{i=1}^{N_v} \frac{\partial \Psi}{\partial \boldsymbol{\epsilon}^{vi}} : \dot{\boldsymbol{\epsilon}}^{vi} + \frac{\partial \Psi}{\partial r} \dot{r} + \frac{\partial \Psi}{\partial r^{nl}} \dot{r}^{nl} + \frac{\partial \Psi}{\partial D} \dot{D} + \frac{\partial \Psi}{\partial \boldsymbol{\nabla}_x r^{nl}} . \left(\boldsymbol{\nabla}_x \dot{r}^{nl} \right) \right) \geq 0. \end{aligned} \tag{19}$$

As seen in the above equation, the nonlocal terms are canceled out, and the dissipation inequality is simply expressed as:

$$\mathcal{D} = \sum_{i=1}^{N_v} \boldsymbol{\sigma}^{vi} : \dot{\boldsymbol{\epsilon}}^{vi} + \boldsymbol{\sigma} : \dot{\boldsymbol{\epsilon}}^{vp} - R\dot{r} + Y\dot{D} \geq 0, \quad \text{with} \quad R = \frac{\partial \Psi}{\partial r}, \; -Y = \frac{\partial \Psi}{\partial D}. \tag{20}$$

It is worth mentioning that the $\dot{D}$ has an implicit dependence on the nonlocal part of the free energy through the hardening term, R. In other words, the damage is driven by plasticity, and $\dot{D}$ directly depends on $\dot{r}$ through the evolution laws, where $\dot{r}$ is affected by R through the von-Mises criterion (1).

The evolution laws are extracted from the convex dual dissipation and indicative functions based on the Generalized Standard Materials formalism (Halphen & Nguyen, 1975) and listed in the table 1. The viscoelastic strain rates can be obtained with respect to their related thermodynamic forces, $\boldsymbol{\sigma}^{vi}$, using the set of sub-potentials, Ω^{vi}:

$$\Omega^{vi} \left(\boldsymbol{\sigma}^{vi}, D \right) = \frac{1}{2} \boldsymbol{\sigma}^{vi} : \frac{\mathbb{V}^{vi\,-1}}{1 - D} : \boldsymbol{\sigma}^{vi}, \tag{21}$$

where $\mathbb{V}^{vi}$ is the viscosity tensor associated with the i-th Kelvin-Voigt branch. The viscoplastic evolution laws coupled with damage are derived based on the J_2-viscoplasticity theory (Chaboche,

1997) through the normality rules by defining identification functions as, F and f_D:

$$F = f(\boldsymbol{\sigma}, -R; D, r) + f_D(Y, D), \quad \text{with} \quad f_D = \frac{S_D}{(\beta_D + 1)(1 - D)} \left(\frac{Y}{S_D} \right)^{\beta_D + 1}, \tag{22}$$

where, here, β_D and S_D denote the damage related model parameters.

So far, the constitutive laws of the matrix phase, as well as the Euler-Lagrange equations, have been discussed. In this respect, the material properties and corresponding model parameters are shown in table 2. In the following sections, an appropriate multi-scale framework is proposed to model the global mechanical response of glass reinforced polyamide 66.

2.2. Multi-scale modeling

This section discusses the nonlocal multi-scale framework for the aforementioned composite. In a composite medium exhibiting nonlocal phenomena, three sizes are of great importance: the global size of the structure, L, the RVE size, l^{ε}, and the nonlocal length scale, l^{nl} of the matrix phase. Assuming that the RVE size is always much smaller than the actual size of the structure ($L \gg l^{\varepsilon}$), two different cases will be examined:

- first, when the RVE size is larger or comparable with the nonlocal length scale ($l^{nl} \leq l^{\varepsilon}$ or l^{nl} in the same order with l^{ε})
- second, when the length scale is much bigger than the RVE size ($l^{nl} \gg l^{\varepsilon}$)

To illustrate the differences between the two cases in terms of homogenized response, several examples of a fiber composite medium will be discussed. For this composite, the RVE is periodic and appears in two different settings: first, as a single periodic unit cell, and second, as a group of periodic unit cells (Fig. 1). The fibers are assumed long, unidirectional, elastic and made of glass, while the matrix phase is of the polyamide 66 material, whose constitutive law has been described in the previous section. For each case, the damage behavior is studied and the analysis is performed using a commercial finite element (FE) tool. Quadratic tetrahedral elements are used in the finite element models, and the numerical implementation of the nonlocal model is expressed in the following sections. For computational reasons, both the matrix and the fibers are assumed to have the same ξ^{nl}, but the γ^{nl} parameter of the fibers is considered zero. The latter hypothesis ensures that the nonlocal field does not present jumps inside the fiber, but also it does not affect its response. The FE size for all these studied cases is approximately $0.05\,mm$, whereas the RVE size is $1\,mm \times 1\,mm \times 0.1\,mm$.

Table 1: State and evolution laws for the viscoelastic viscoplastic material (Praud et al., 2017a) ($\dot{\lambda}$, $\mathbf{\Lambda}_{vp}$, and Λ_D are viscoplastic multiplier, plastic flow, and damage direction respectively.)

State variable	Conjugate variable	Evolution laws
strain tensor, $\boldsymbol{\epsilon}$	$\boldsymbol{\sigma}=\dfrac{\partial \Psi}{\partial \boldsymbol{\epsilon}}$	
Viscoelastic strains, $\boldsymbol{\epsilon}^{vi}$	$-\boldsymbol{\sigma}^{vi} = \dfrac{\partial \Psi}{\partial \boldsymbol{\epsilon}^{vi}}$ $= (1-D)\mathbb{C}^{vi} : \boldsymbol{\epsilon}^{vi} - \boldsymbol{\sigma}$	$\dot{\boldsymbol{\epsilon}^{vi}} = \dfrac{\partial \Omega^{vi}}{\partial \boldsymbol{\sigma}^{vi}} = \dfrac{(\mathbb{V}^{vi})^{-1}}{1-D} : \boldsymbol{\sigma}^{vi}$
Viscoplastic strain, $\boldsymbol{\epsilon}^{vp}$	$-\boldsymbol{\sigma} = \dfrac{\partial \Psi}{\partial \boldsymbol{\epsilon}^{vp}}$	$\dot{\boldsymbol{\epsilon}^{vp}} = \dfrac{\partial F}{\partial \boldsymbol{\sigma}}\dot{\lambda} = \Lambda_{vp}\dot{\lambda}$
Hardening state variable, r	R$=\dfrac{\partial \Psi}{\partial r} = R^l + R^{nl}$ $R^l = H_m\, r^{H_p}$, $R^{nl} = \gamma^{nl}(r - r^{nl})$	$\dot{r} = \dot{\lambda}$
Damage, D	$-Y = \dfrac{\partial \Psi}{\partial D}$	$\dot{D} = \dfrac{\partial F}{\partial Y}\dfrac{\dot{\lambda}}{1-D} = \Lambda_D \dot{\lambda}$
Nonlocal hardening state variable, r^{nl}	$Y_{r^{nl}} = \dfrac{\partial \Psi}{\partial r^{nl}}$	-
Gradient of the nonlocal variable, $\boldsymbol{\nabla}_x r^{nl}$	$\boldsymbol{Y}_{\boldsymbol{\nabla}_x r^{nl}} = \dfrac{\partial \Psi}{\partial \boldsymbol{\nabla}_x r^{nl}}$	-

Table 2: Material properties and model parameters for PA66 at RH50% (Relative Humidity) and room temperature (Benaarbia et al., 2019).

Mechanical feature	**parameter**	**Value (unit)**
Elastic properties:		
Young's modulus	E^e	2731 (MPa)
Poisson ratio	ν	0.3 (-)
Viscoelasticity:		
1^{st} branch:	E^{v1}	9751.44 (MPa)
	τ^{v1}	0.36 (s)
2^{nd} branch:	E^{v2}	19125.64 (MPa)
	τ^{v2}	6.72 (s)
3^{th} branch:	E^{v3}	30855.24 (MPa)
	τ^{v3}	6.38 (s)
4^{th} branch:	E^{v4}	6771.25 (MPa)
	τ^{v4}	128.49 (s)
Viscoplasticity coupled with damage:		
Elastic limit:	R_0	4.76 (MPa)
Hardening model:	H_m	1302.71 (MPa)
	H_p	0.8 (MPa)
Viscoplastic model:	R_{vp}	45.86 (MPa .s$^{P_{vp}}$)
	P_{vp}	0.07 (-)
Damage:	S_D	20.03 (MPa)
	β_D	-0.86 (-)

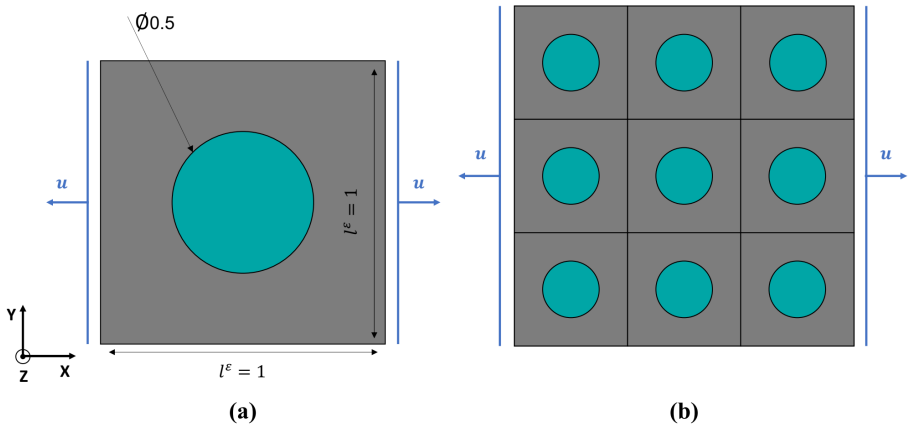

Figure 1: Loading conditions ($\dot{\boldsymbol{u}} = 0.1\,mms^{-1}$) and the dimensions corresponding to: a) single long fiber reinforced RVE, b) a group of RVEs (dimensions are based on mm); the thickness for both cases is $0.1\,mm$.

2.2.1. Case 1: $l^{nl} \leq l^{\varepsilon}$ or l^{nl} in the same order with l^{ε}

In this case, the nonlocal length scale, l^{nl}, is assumed to be smaller than or in the same order with the RVE size, l^{ε}. This assumption implies that the nonlocal length scale is not present explicitly at the macroscale and only appears at the microscale. Accordingly, the multi-scale system of equations can be derived using asymptotic expansion as:

- macroscale:

$$\frac{\partial \bar{\sigma}_{ij}}{\partial \bar{x}_i} = 0 \quad \text{with} \quad \langle \sigma_{ij}^{(0)} \rangle = \bar{\sigma}_{ij}, \tag{23}$$

- microscale:

$$\begin{cases} \dfrac{\partial \sigma_{ij}^{(0)}}{\partial x_i} = 0, \\ \xi^{nl} \dfrac{\partial}{\partial x_i} \left(\dfrac{\partial r^{nl}}{\partial x_i} \right) + \gamma^{nl} \left(r - r^{nl} \right) = 0, \end{cases} \tag{24}$$

where the symbols, "$\bar{.}$" and "$\langle . \rangle$", are the macroscopic variable and the average on the microscopic unit cell volume respectively, and "$.^{(0)}$" and "$.^{(1)}$" are zero and first order terms of the corresponding asymptotic expansion. The deriving procedure is fully expressed in Appendix A. It is noted that such case may be problematic from a homogenization point of view. As it has been reported in the literature (Fantoni et al., 2020).

As a first example, the periodic boundary conditions with the loading conditions given in Fig. 1 are applied on a single RVE and a group of RVEs when $l^{nl} = 0.01\, l^{\varepsilon}$, and the resulting damage profiles are extracted in Fig. 2. As a matter of fact, since the length scale determines the influencing zone of the nonlocal regularization, for a smaller length scale, the damage profile localizes into a narrower region. As seen, the damage profiles are not identical and uniform in the RVEs set. This arises questions whether the periodicity assumption is valid. As the second example, the same analysis is performed when $l^{nl} = 0.1\, l^{\varepsilon}$, and the 3D maps of damage are depicted in Fig. 3. As observed, by increasing the ratio of l^{nl}/l^{ε}, the damage profiles become almost uniform in the RVEs group, and the damage stays within the RVE and concentrates around the fiber.

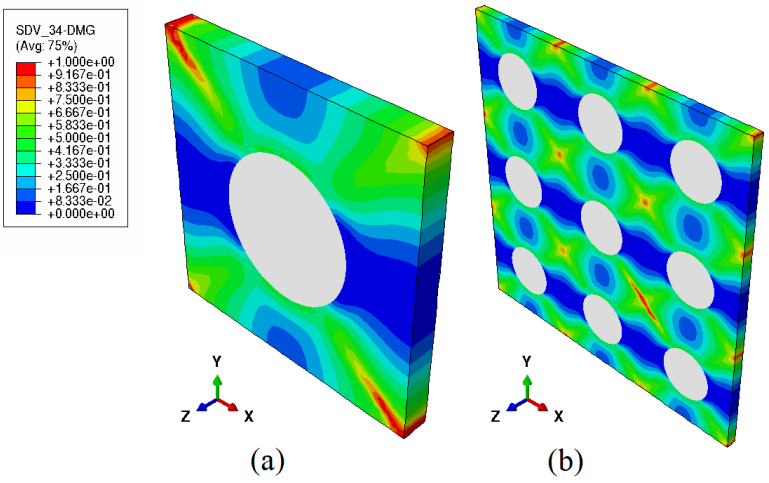

Figure 2: Damage profile under $0.1\, mms^{-1}$ monotonic loading rate when $l^{nl} = 0.01\, l^{\varepsilon}$ in a) single long fiber reinforced RVE, b) a group of RVEs. Element size is set to $0.05\, mm$.

2.2.2. Case 2: $l^{nl} \gg l^{\varepsilon}$

As the second case, the nonlocal length scale is assumed to be much larger than the RVE size. Therefore, the nonlocal equation does not appear at the micro level and passes through the macroscale. Based on the asymptotic expansion given in Appendix A, it is shown that the scale separation has a more "classical" formalism, and the governing equations at the macro and micro scales are expressed as follows:

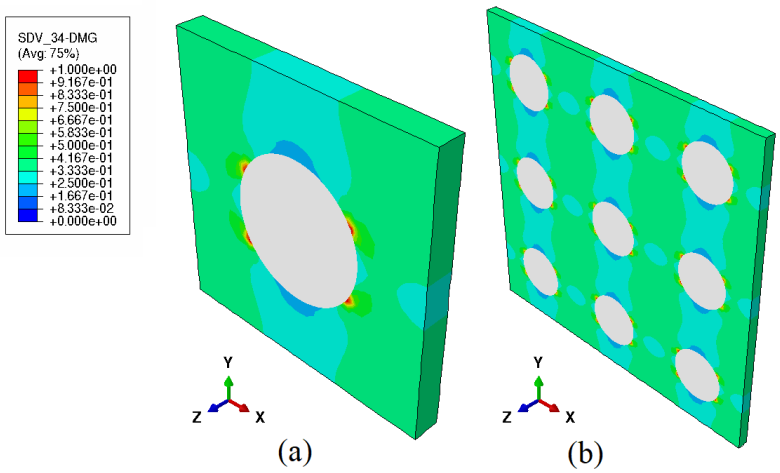

Figure 3: Damage profile under $0.1\,mms^{-1}$ monotonic loading rate using the nonlocal model when $l^{nl} = 0.1\,l^{\varepsilon}$ in a) single short fiber reinforced RVE, b) a group of RVEs. Element size is set to $0.05\,mm$.

- macroscale:

$$\begin{cases} \dfrac{\partial \bar{\sigma}_{ij}}{\partial \bar{x}_i} = 0 \quad \text{with} \quad \langle \sigma_{ij}^{(0)} \rangle = \bar{\sigma}_{ij}, \\ \xi^{nl} \dfrac{\partial}{\partial \bar{x}_i} \left(\dfrac{\partial r^{nl(0)}}{\partial \bar{x}_i} \right) + \langle \gamma^{nl} r^{(0)} \rangle - \langle \gamma^{nl} \rangle r^{nl(0)} = 0, \end{cases} \tag{25}$$

- microscale

$$\frac{\sigma_{ij}^{(0)}}{\partial x_i} = 0. \tag{26}$$

Similar example with the previous one, considering this time $l^{nl} = 100\,l^{\varepsilon}$, allows to study the damage growth within the RVEs (see Fig. 4). As observed, the RVEs damage profiles are identical, and the periodicity assumption within the RVEs set is fully satisfied.

According to the above results, it can be concluded that the second case ($l^{nl} \gg l^{\varepsilon}$) is more compatible with the multi-scale framework than the first one because it satisfies the periodicity assumption and the classical scale separation formalism. Furthermore, this assumption allows the nonlocal variable to be identical throughout the RVE, whereas smaller length scales lead to non-uniform nonlocal variable, r^{nl}, at the microscale. This fact is confirmed through 3D maps of the

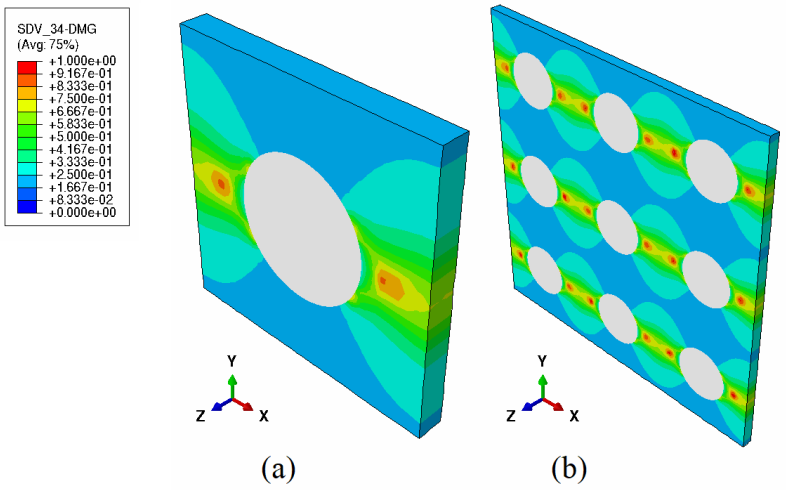

Figure 4: Damage profile under $0.1\,mms^{-1}$ monotonic loading rate using the nonlocal model when $l^{nl} = 100\,l^{\varepsilon}$ in a) single short fiber reinforced RVE, b) a group of RVEs. Element size is set to $0.05\,mm$.

nonlocal variable, r^{nl}, depicted in Fig. 5. Uniform nonlocal variable within the RVE makes the model compatible with the mean field homogenization frameworks, in which the material properties in the RVE vary by phase. In addition, the second case is more acceptable physically because the localization of state variables, particularly damage, is a problem of the macroscale failure.

It is worth mentioning that, according to nonlocal analyses standards (Seupel et al., 2018; Navidtehrani et al., 2021), for $l^{nl} = 0.1\,l^{\varepsilon}$ and $l^{nl} = 100\,l^{\varepsilon}$, the FE size is sufficiently small compared to the length scales. However, for the lowest l^{nl} case, this FE size is relatively large. An additional analysis with much finer mesh leads to qualitatively similar results, confirming thus the derived conclusions of the study.

2.3. Mori-Tanaka/TFA framework

Since the focus of this research is the failure at the macrostructure, the second case (i.e. $l^{nl} \gg l^{\varepsilon}$) is considered to develop the multi-scale framework. The conclusions reached from the asymptotic expansion homogenization approach, specially with regard to the macroscale and microscale problems, can be adopted for other micromechanics schemes. Mori-Tanaka/TFA homogenization approach is used here to model overall mechanical responses of glass fiber reinforced polyamide 66.

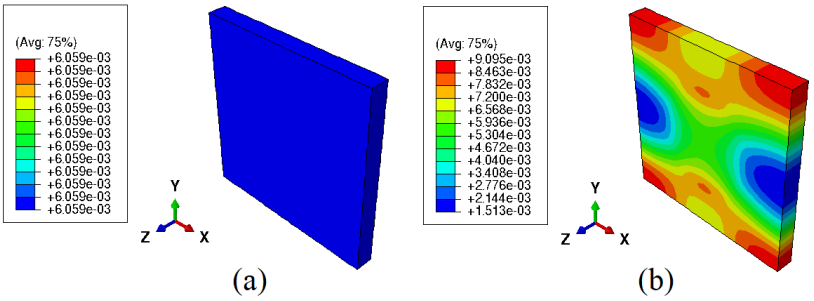

Figure 5: Nonlocal variable, r^{nl}, profile under periodic boundary conditions when a) $l^{nl} = 100\, l^{\varepsilon}$, b) $l^{nl} = 0.1\, l^{\varepsilon}$.

Since the current work is an attempt to establish a general framework and there is no experimental comparison, the classical Mori-Tanaka/TFA framework without inelasticity related modifications is adopted here. The proposed theory can be easily extended to adopt a correction on the plastic strains level. Mori-Tanaka/TFA method suggests splitting the total macroscopic stress into two parts, elastic and inelastic (Dvorak & Benveniste, 1992; Chen et al., 2021; Chatzigeorgiou et al., 2022):

$$\bar{\boldsymbol{\sigma}} = \bar{\boldsymbol{\sigma}}^{r} + \bar{\boldsymbol{\sigma}}^{in} = \bar{\mathbb{C}}^{sec} : \bar{\boldsymbol{\epsilon}} + \bar{\boldsymbol{\sigma}}^{in}, \tag{27}$$

where $\bar{\mathbb{C}}^{sec}$ is the 4th order secant tensor, and the superscripts ".^{e}" and ".^{in}" respectively denote the elastic and inelastic parts of the variable. Based on the extended Eshelby's problem the inclusion deformation, $\boldsymbol{\epsilon}_1$ is defined as (Chatzigeorgiou & Meraghni, 2019):

$$\boldsymbol{\epsilon}_1 = \boldsymbol{T}_1 : \boldsymbol{\epsilon}_0 + \boldsymbol{T}_1^{p} : \boldsymbol{\sigma}_0^{in} - \boldsymbol{T}_1^{p} : \boldsymbol{\sigma}_1^{in} \tag{28}$$

with

$$\boldsymbol{T}_1 = [\boldsymbol{I} + \boldsymbol{P} : (\mathbb{C}_1^{sec} - \mathbb{C}_0^{sec})]^{-1}, \quad \boldsymbol{T}_1^{p} = \boldsymbol{T}_1 : \boldsymbol{P}, \quad \boldsymbol{P} = \boldsymbol{S}\,(\mathbb{C}_0^{sec}) : \mathbb{C}_0^{sec\,-1}, \tag{29}$$

where $\boldsymbol{S}$ is the Eshelby tensor; here, the subscripts, ".$_0$" and ".$_1$", denote the matrix and inclusion variables, and $\boldsymbol{T}_1$ and $\boldsymbol{T}_1^{p}$ are the elastic and inelastic interaction tensors respectively. The macroscopic strain, $\bar{\boldsymbol{\epsilon}}$, for a composite material whose RVE constitutes from the matrix phase and one

single inclusion is expressed as:

$$\bar{\boldsymbol{\epsilon}} = V_0^f \boldsymbol{\epsilon}_0 + V_1^f \boldsymbol{\epsilon}_1. \tag{30}$$

where V_0^f and V_1^f are the matrix and inclusion volume fractions respectively. Substituting (28) into (30) yields:

$$\bar{\boldsymbol{\epsilon}} = V_0^f \boldsymbol{\epsilon}_0 + V_1^f \left(\boldsymbol{T}_1 : \boldsymbol{\epsilon}_0 + \boldsymbol{T}_1^p : \boldsymbol{\sigma}_0^{in} - \boldsymbol{T}_1^p : \boldsymbol{\sigma}_1^{in} \right), \tag{31}$$

where it can be rewritten as:

$$\bar{\boldsymbol{\epsilon}} = \left(V_0^f \boldsymbol{I} + V_1^f \boldsymbol{T}_1 \right) : \boldsymbol{\epsilon}_0 + V_1^f \left(\boldsymbol{T}_1 : \boldsymbol{\sigma}_0^{in} - \boldsymbol{T}_1^p : \boldsymbol{\sigma}_1^{in} \right), \tag{32}$$

Thus, the matrix deformation can be expressed as:

$$\boldsymbol{\epsilon}_0 = \boldsymbol{A}_0 : \bar{\boldsymbol{\epsilon}} + \boldsymbol{A}_0^p : \boldsymbol{\sigma}_0^{in} + \boldsymbol{A}_1^p : \boldsymbol{\sigma}_1^{in} \tag{33}$$

with the concentration tensors being given by the formulas:

$$\boldsymbol{A}_0 = \left[V_0^f \boldsymbol{I} + V_1^f \boldsymbol{T}_1 \right]^{-1}, \quad \boldsymbol{A}_0^p = -V_1^f \boldsymbol{A}_0 : \boldsymbol{T}_1^p, \quad \boldsymbol{A}_1^p = \boldsymbol{A}_0 : V_1^f \boldsymbol{T}_1. \tag{34}$$

The inclusion deformation is also derived by substituting (33) into (28):

$$\boldsymbol{\epsilon}_1 = \boldsymbol{A}_1 : \bar{\boldsymbol{\epsilon}} + \boldsymbol{A}_0^f : \boldsymbol{\sigma}_0^{in} + \boldsymbol{A}_1^f : \boldsymbol{\sigma}_1^{in}, \tag{35}$$

with

$$\boldsymbol{A}_1 = \boldsymbol{T}_1 : \boldsymbol{A}_0, \quad \boldsymbol{A}_0^f = \boldsymbol{T}_1 : \boldsymbol{A}_0^p + \boldsymbol{T}_1^p, \quad \boldsymbol{A}_1^f = \boldsymbol{T}_1 : \boldsymbol{A}_1^p - \boldsymbol{T}_1^p. \tag{36}$$

The overall stiffness for the present two phase composite is defined as (Dvorak & Benveniste, 1992):

$$\bar{\mathbb{C}}^{sec} = V_0^f \mathbb{C}_0^{sec} : \boldsymbol{A}_0 + V_1^f \mathbb{C}_1^{sec} : \boldsymbol{A}_1. \tag{37}$$

Since the glass fibers are considered elastic, $\boldsymbol{\sigma}_1^{in} = 0$, and the $\boldsymbol{A}_1^p$ and $\boldsymbol{A}_1^f$ concentration tensors can be omitted in the computational procedure. Moreover, the secant modulus, $\mathbb{C}_1^{sec}$, coincides with the elastic modulus of the reinforcement.

The next section deals with the numerical implementation of the present multi-scale model, combining the VEVPD matrix phase, the homogenization scheme, and the nonlocal framework.

3. Numerical implementation

The numerical implementation consists of three different stages: first, the microscale inelastic mechanisms in the matrix phase are computed and updated using a VEVPD subroutine, second, the micromechanical model subroutine providing the global stress tensor and secant modulus, and third, the nonlocal part implemented at the macroscopic scale using the analogy between heat and nonlocal equations through HETVAL subroutine. It is worth mentioning that in recent versions of ABAQUS (not older than 2020), the analogy of the nonlocal and heat equations can also be implemented on the finite element model using only a user material subroutine (UMAT) and four types of tangent moduli (Navidtehrani et al., 2021). However, in this study, the HETVAL subroutine is employed for resolving the coupled system of equations.

The interaction between the stages mentioned above and the associated inputs and outputs are briefly presented as a flowchart in Fig. 6. The following sections discuss each part of the implementation procedure in more detail.

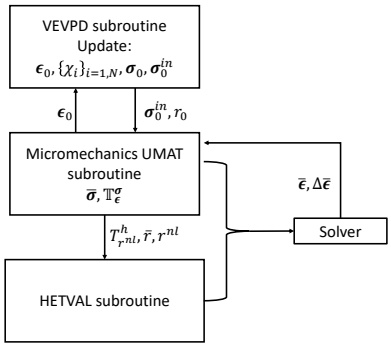

Figure 6: Flowchart of the numerical implementation in ABAQUS FE software for a composite structure. It should be mentioned that the HETVAL subroutine only needs $T_h^{r^{nl}}$, as the associated nonlocal tangent operator.

3.1. VEVPD model numerical implementation

The VEVPD numerical model is discretized in time based on an implicit backward Euler scheme compatible with the FE solver inputs in time steps. The associated subroutine takes the total deformation of the matrix phase, $\boldsymbol{\epsilon}_0$, at the time step n, and the corresponding deformation variation,

$\Delta\boldsymbol{\epsilon}_0$, at the time step $n+1$, as inputs and produces the inelastic stress, $\boldsymbol{\sigma}_0^{in}$, and the secant modulus of the matrix phase, $\mathbb{C}_0^{sec}$, as outputs. For updating the internal state variables and calculating the inelastic stress, an iterative process is designed based on the "convex cutting plane" return mapping algorithm (Qidwai & Lagoudas, 2000; Simo & Hughes, 2006). As an efficient method, the algorithm is divided into two steps: viscoelastic correction-prediction and full correction. At the first stage, no plasticity or damage is taken into account, and the deformation is governed by viscoelasticity. Therefore, only the total strain and viscoelastic strain elements vary under deformation. Once the equivalent stress, σ^{eq}, exceeds the material elastic limit, R_0 ($f > 0$), the viscoplastic and damage mechanisms are activated, and a full correction is required to update the state variables including viscoplastic strain, hardening state variables, and viscoelastic strains. More detailed description of the numerical implementation of the VEVPD model can be found in Praud et al. (2017a).

3.2. Micromechanics model algorithm

The goal of the micromechanical model is to provide the solver with the overall stress and secant modulus tensors in macroscopic scale. To this end, the micromechanical subroutine passes the matrix phase strain tensor, $\boldsymbol{\epsilon}_0$ and its corresponding variation, $\Delta\boldsymbol{\epsilon}_0$, to the VEVPD tool which yields the inelastic stress tensor, $\boldsymbol{\sigma}_0^{in}$. Since the matrix deformation depends on the inelastic mechanisms (equation (33)), an iterative algorithm is adopted to calculate the inelastic stress tensor. Table 3 provides the detailed description of the numerical micromechanical UMAT as an algorithm box. Also, Fig. 6 illustrates how the numerical tools are inter-connected.

3.3. Nonlocal model setup within the ABAQUS FE software

As mentioned in the previous sections, the nonlocal phenomena appear and are integrated at the macroscopic scale. In this regard, the nonlocal strategy uses ξ^{nl} and $\langle\gamma^{nl}\rangle$ as nonlocal parameters. Also, it passes as inputs to the solver: the average local quantity, $\langle\gamma^{nl}\, r\rangle$, and the nonlocal variable, r^{nl}, as well as the associated tangent operators. In this respect, since the present gradient enhanced model contains the nonlocal balance equation as well as the stress equilibrium, an additional degree of freedom must be defined as the nonlocal field. To this end, there are two main approaches suggested in the literature. The first approach is to develop a User defined Element (UEL) subroutine (Dimitrijevic & Hackl, 2011; Kiefer et al., 2018), which besides the visualization complexities also requires significant additional programming. The second approach is to use the

Table 3: Algorithm box: Micromechanics iteration algorithm

1- Recover stress and state variables at the time step, n:

$\boldsymbol{\epsilon}_0^{vp(n)}$, $\boldsymbol{\epsilon}_0^{vi(n)}$, $D_0^n, r_0^n, \boldsymbol{\epsilon}_0^n, \boldsymbol{\epsilon}_1^n, \boldsymbol{\sigma}_0^n, \boldsymbol{\sigma}_0^{in(n)}$ with $(i = 1, .., N_v)$.

2- Calculate secant modulus tensors:

$\mathbb{C}_0^{sec}$, $\mathbb{C}_1^{sec}$.

3- Calculate concentration tensors based on $\mathbb{C}_0^{sec}$, $\mathbb{C}_1^{sec}$:

$\boldsymbol{A}_0$, $\boldsymbol{A}_0^p$, $\boldsymbol{A}_1$.

5- Compute $\Delta\boldsymbol{\epsilon}_0$ using concentration tensors:

$\Delta\boldsymbol{\epsilon}_0 = \boldsymbol{\epsilon}_0^{n+1} - \boldsymbol{\epsilon}_0^n = \boldsymbol{A}_0 : (\bar{\boldsymbol{\epsilon}} + \Delta\bar{\boldsymbol{\epsilon}}) + \boldsymbol{A}_0^p : \boldsymbol{\sigma}_0^{in} - \boldsymbol{\epsilon}_0^n$.

Start iterative process.

6- Run VEVPD subroutine and update:

$\boldsymbol{\epsilon}_0^{vp(n)}$, $\boldsymbol{\epsilon}_0^{vi(n)}$, $D_0^n, r_0^n, \boldsymbol{\epsilon}_0^n, \boldsymbol{\epsilon}_1^n, \boldsymbol{\sigma}_0^n, \boldsymbol{\sigma}_0^{in(n)}$ with $(i = 1, .., N_v)$.

7- Update secant modulus tensor, $\mathbb{C}_0^{sec}$, and concentration tensors:

$\boldsymbol{A}_0$, $\boldsymbol{A}_0^p$, $\boldsymbol{A}_1$.

8- Update $\Delta\boldsymbol{\epsilon}_0$ and $\Delta\boldsymbol{\epsilon}_1$ corresponding to iteration step $k+1$:

$\Delta\boldsymbol{\epsilon}_0^{k+1} = \boldsymbol{\epsilon}_0^{n+1} - \boldsymbol{\epsilon}_0^n = \boldsymbol{A}_0 : (\bar{\boldsymbol{\epsilon}} + \Delta\bar{\boldsymbol{\epsilon}}) + \boldsymbol{A}_0^p : \boldsymbol{\sigma}_0^{in} - \boldsymbol{\epsilon}_0^n$,

$\Delta\boldsymbol{\epsilon}_1^{k+1} = (\Delta\bar{\boldsymbol{\epsilon}} - V_0^f \Delta\boldsymbol{\epsilon}_0)/V_1^f$.

9- Update concentration tensors.

10- if $\left||\Delta\boldsymbol{\epsilon}_0^{k+1} - \Delta\boldsymbol{\epsilon}_0^k|\right| + \left||\Delta\boldsymbol{\epsilon}_1^{k+1} - \Delta\boldsymbol{\epsilon}_1^k|\right| \leq R^{tol}$,

update $\boldsymbol{\epsilon}_0$, $\boldsymbol{\epsilon}_1$, $\boldsymbol{\sigma}_0$, $\boldsymbol{\sigma}_1$, $\bar{\boldsymbol{\sigma}}$,

else set $k = k + 1$ and return to 6,

11- Compute the tangent modulus (stiffness tensors) of each phase,

12- Calculate concentration tensors using the tangent moduli of the phases,

13- Compute the overall stiffness tensor, $\mathbb{T}_{\boldsymbol{\epsilon}}^{\boldsymbol{\sigma}}$, using (37).

fully coupled temperature displacement analysis tools in ABAQUS through the analogy between the nonlocal and steady state heat equations (Hortig, 2010; Ostwald et al., 2019):

$$K_c \boldsymbol{\nabla}_x^2 \theta + h_g = 0 \quad \Longleftrightarrow \quad \xi^{nl} \boldsymbol{\nabla}_x^2 r^{nl} + \gamma^{nl} \left(r - r^{nl} \right) = 0, \tag{38a}$$

$$\boldsymbol{q}.\boldsymbol{n} = 0 \quad \Longleftrightarrow \quad \xi^{nl} \boldsymbol{\nabla}_x r^{nl}.\boldsymbol{n} = 0, \tag{38b}$$

where θ, K_c, h_g, and $\boldsymbol{n}$ are respectively the temperature, the corresponding heat conduction, the heat sources, and the unit normal vector to the surface, and $\boldsymbol{q}$ denotes the heat flux vector which can be obtained from the Fourier's law as:

$$\boldsymbol{q} = -K_c \boldsymbol{\nabla}_x \theta. \tag{39}$$

Using the above analogy requires a proper definition of the thermomechanical tangent operators. Therefore, in the present study, HETVAL subroutine is used to meet two targets: first, providing the associated thermomechanical tangent operators for the solver, and second, introducing heat flow, heat sources, and interactions between the corresponding state variables and temperature into the FE model, in which the temperature and its associated fields are replaced by the nonlocal variable and its relevant analogous fields.

3.4. Tangent operators

Based on the governing equations (25), the increment of the overall stress and the associated nonlocal term is expressed as:

$$\Delta \bar{\boldsymbol{\sigma}} = \mathbb{T}_{\boldsymbol{\epsilon}}^{\boldsymbol{\sigma}} : \Delta \bar{\boldsymbol{\epsilon}} + \boldsymbol{T}_{r^{nl}}^{\boldsymbol{\sigma}} \, \Delta r^{nl} \tag{40a}$$

$$\Delta \left[\langle \gamma^{nl} r \rangle - \langle \gamma^{nl} \rangle r^{nl} \right] = \boldsymbol{T}_{\epsilon}^{h} : \Delta \bar{\boldsymbol{\epsilon}} + T_{r^{nl}}^{h} \, \Delta r^{nl} \tag{40b}$$

with

$$\Delta \left[\langle \gamma^{nl} r \rangle - \langle \gamma^{nl} \rangle r^{nl} \right] = V_0^f \gamma_0^{nl} \left(\Delta r - \Delta r^{nl} \right) \tag{41}$$

where $\mathbb{T}_{\varepsilon}^{\boldsymbol{\sigma}}$ denotes the overall stiffness tensor computed using (37) by substituting the phases tangent moduli and the corresponding concentration tensors, and it is passed to the solver through the

UMAT subroutine. In addition, since the inclusion is considered elastic, the parameter γ_1^{nl} is considered zero, however its ξ^{nl} term is assumed the same with that of the matrix phase. Here, $\boldsymbol{T}^{\boldsymbol{\sigma}}_{r^{nl}}$, $\boldsymbol{T}^{h}_{\epsilon}$, and $T^{h}_{r^{nl}}$ are the associated nonlocal tangent operators, of which only $T^{h}_{r^{nl}}$ is required by HETVAL, and simply derived as:

$$T^{h}_{r^{nl}} = -\langle \gamma^{nl} \rangle = -(V_0^f \gamma_0^{nl} + V_1^f \cancelto{0}{\gamma_1^{nl}}) = -V_0^f \gamma_0^{nl}. \tag{42}$$

4. Results and discussion

In this section, the overall mechanical responses of the proposed multi-scale model are studied under small deformation assumption (up to 10%). In this paper, the matrix phase is polyamide 66 with material properties given in table 2, and the inclusions are made of glass (elastic phase) with Young's modulus, $E^g = 72000\,\text{MPa}$, and Poisson's ratio, $\nu^g = 0.22$. In the absence of available experimental data, the Mori-Tanaka/TFA nonlocal homogenization framework is validated through a unilateral notched multi-layered body. The results from the homogenization analysis are compared with a full structure finite element model study. Then the proposed model is examined for a long glass fiber reinforced composite structure (notched plate), and finally, the influences of different parameters are explored as a parametric study for an asymmetrically double notched structure.

4.1. Preliminary validation of the nonlocal model against full-structure solution for multi-layered composite

The validity of the suggested Mori-Tanaka/TFA framework can be investigated using a multi-layered model (Chatzigeorgiou, 2021). In this respect, a unilateral notched body is considered with the geometry and boundary conditions given in Fig. 7-a. Initially, the proposed homogenization scheme is implemented on the structure subjected to a monotonic load on the external surfaces normal to Y-axis (Fig. 7-a), then the obtained results are compared to a complete structural model without homogenization (Fig. 8-a), consisting of 100 RVEs. In terms of boundary conditions, the base of the structure is fixed and the monotonic load is imposed from above. Each RVE is constituted from a polymer layer in the middle and two glass layers at the sides, in which the glass volume fraction is set as 20 percent (see Fig. 8-b). The number of layers determines the size of RVE which should be much smaller than the considered length scale as discussed in the past sections. Here, the nonlocal parameters are given as $\gamma^{nl} = 5\,\text{GPa}$ (for the matrix) and $\xi^{nl} = 600\,\text{kN}$ ($l^{nl^2} = \xi^{nl}/\gamma^{nl}$),

while the ratio between length scale and the RVE size is derived based on the number of RVEs in the structure which means $l^{nl}/l^{\varepsilon} \approx 36.51$. The convergence analysis has already been performed in our previous work (Satouri et al., 2022), and since here the main focus is to present a suitable nonlocal homogenization framework, it has not been discussed in this paper. Fig. 9 shows von Mises stress and damage distribution of the multi-layered structure and exhibits how the combination of the glass and polyamide 66 layers responds under loading. The responses of both models under the same boundary conditions are extracted as displacement force curves in Fig. 10. As observed, there is a good agreement between the two analyses.

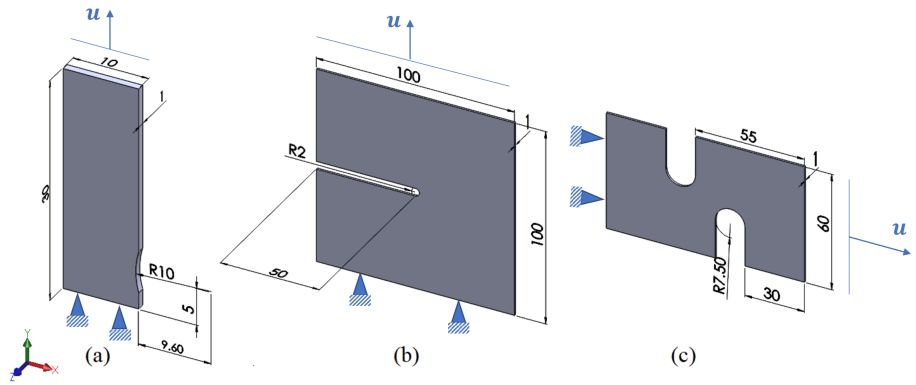

Figure 7: Geometrical dimensions and the corresponding boundary conditions of: a) unilateral notched plate, b) plate with a long notch, and c) asymmetrically double notched structure.

4.2. Comparison of local and nonlocal models for long glass fiber reinforced structure

In this section, a composite notched plate is subjected to a monotonic tensile test, whose dimensions are given in Fig. 7-b. The composite is considered as unidirectional long glass fiber reinforced polyamide 66, and its overall mechanical behavior is estimated using the latter homogenization framework based on single fiber RVEs, oriented in Z direction. The given structure is pulled from the upper side and fixed at the bottom, and the strain controlled loading rate is assigned to 5 $mm\,\mathrm{s}^{-1}$ (Fig. 7-b). Based on the present specified boundary conditions, local and nonlocal models

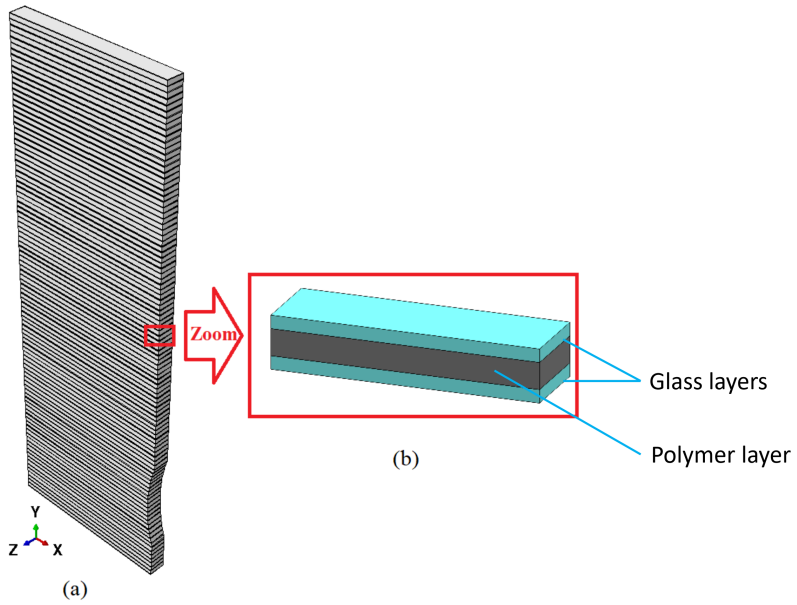

Figure 8: a) Multi-layered unilateral structure; b) zoom view and configuration of each RVE. The element type is the coupled temperature-displacement brick element (C3D8T).

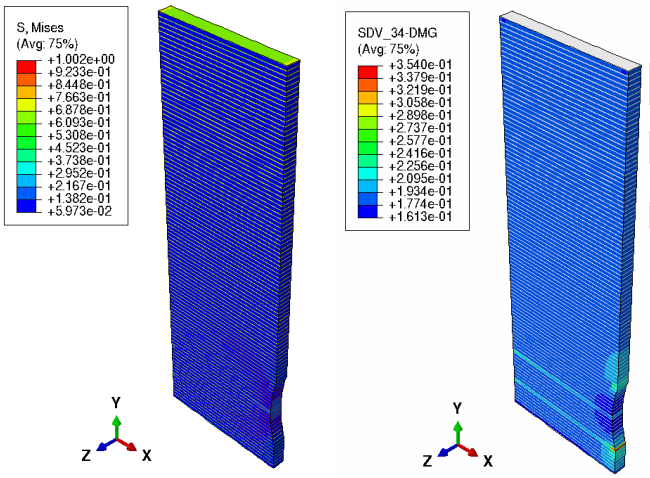

(a) von Mises stress 3D map (b) Damage 3D map

Figure 9: 3D maps of von Mises stress and damage under $5\,mm\mathrm{s}^{-1}$ monotonic loading rate in the multi-layered structure when $l^{nl}/l^{\varepsilon} \approx 36.51$. The element type is the coupled temperature-displacement brick element (C3D8T).

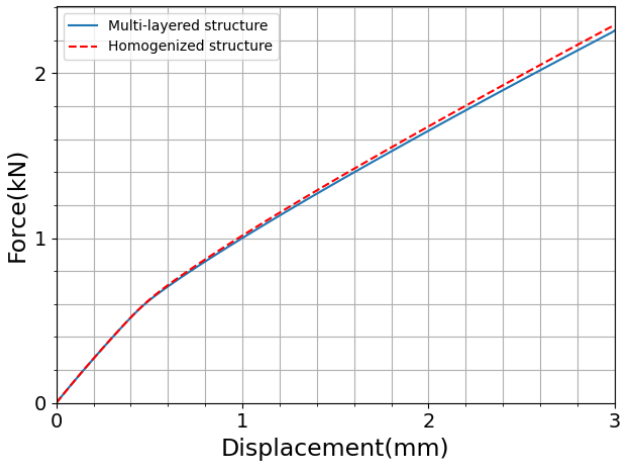

Figure 10: Force-displacement curve under $1.5\,mm\,\mathrm{s}^{-1}$ monotonic loading rate for multi-layered and homogenized unilateral notched structure using the nonlocal framework when $l^{nl}/l^{\varepsilon} \approx 36.51$, $\xi^{nl} = 600\,\mathrm{kN}$, and $\gamma^{nl} = 5\,\mathrm{GPa}$.

are implemented into a commercial finite element software, and the mechanical responses are investigated. Fig. 11 compares the force-displacement curves between local and nonlocal models. As shown, after some point, the nonlinear part of the curves in the local and nonlocal continuum models diverge, and the local model fails at a lower force level while the nonlocal model keeps evolving in a more stable way. Fig. 12 shows the 3D maps of the matrix damage for the local and nonlocal models. As observed, in local models, the damage is localized in the crack zone passing through the structure. However in the nonlocal model, the damage remains around the notch region. In other words, the nonlocal model yields more stable responses in the small deformation zone compared the local framework. It should be mentioned that the maximum damage location from the "concentrator" depends on the length scale. In the example of the plate with a long notch, where the notch plays the role of the "concentrator", one can see that the maximum damage location has a certain distance from the notch, as shown in Fig. 12. The notched plate is considered under the same boundary conditions, and the subsequent analysis is performed with different values of the nonlocal parameters when the nonlocal length scale is held constant. The resulting 3D damage maps are presented in Figure 13 for four sets of nonlocal parameters. As observed, changing the nonlocal parameters can invert the damage patterns. Consequently, the proposed model can lead to different damage profiles. Verification of the correct nonlocal parameters can be achieved through proper calibration against experimental data.

4.3. Parametric study

In this section, a parametric study is conducted to explore the effect of nonlocal parameters, volume fraction, and loading rates. To this end, an asymmetrically double notched structure is considered, whose dimensions are given in Fig. 7-c. The boundary conditions are imposed on the external surfaces normal to X-axis (Fig. 7-c). The displacement field is set to zero on one side, and a strain-controlled load is applied on the other side. As the previous section, the homogenization framework is implemented based on the RVEs containing single long glass fiber, parallel to Z-axis, and the responses are conducted in different cases and compared with each other. Fig. 14 shows the force-displacement curves in the different glass fiber volume fractions under a loading rate of 5 $mm\,\mathrm{s}^{-1}$ ($\gamma^{nl} = 5\,\mathrm{GPa}$, $\xi^{nl} = 80\,\mathrm{kN}$). As expected, the higher the volume fraction of glass fibers, the stiffer the structure becomes. Fig. 15 shows more clearly how the volume fraction affects the stress level in the structure. As seen, for higher volume fractions, higher von Mises stress values are

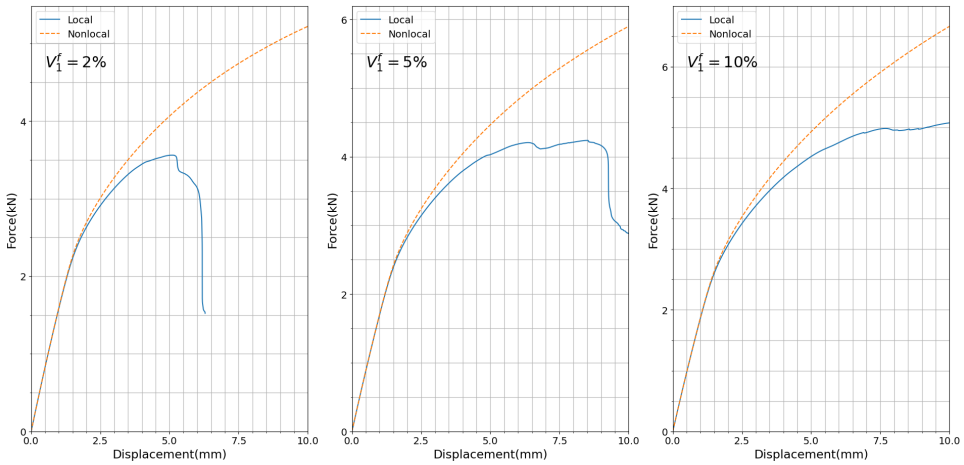

Figure 11: Force-displacement curves for the composite notched plate under $5\,mm\,s^{-1}$ monotonic loading rate using local and nonlocal models with $\xi^{nl} = 80\,kN$ and $\gamma^{nl} = 5\,GPa$ when $V_1^f = 2\%$, $V_1^f = 5\%$, and $V_1^f = 10\%$. The element type is the coupled temperature-displacement brick element (C3D8T).

observed. For the latter analysis, matrix damage profiles are also provided as Fig. 16. As shown, the level of damage around the notches is quite high, and its concentration increases when the glass volume fracture is larger. Since the matrix phase is a viscoelastic viscoplastic material (polyamide 66), the loading rate influences the material responses. In this respect, results at different loading rates are extracted for the composite with 10 percent glass fiber volume fraction, and the nonlocal parameters are given as $\gamma^{nl} = 5\,GPa$, $\xi^{nl} = 80\,kN$ (see Fig. 17). As observed, higher loading rates lead to higher slope curves and stiffer material behavior. However, the loading rate effect is more pronounced when the rate is increased to $50\,mm\,s^{-1}$. Figs.14, 15, and 17 imply that the impact of inclusion volume fraction and the loading rate on the composite mechanical behavior conforms to the expectations, and the present nonlocal framework does not violate them.

As discussed in the previous section, the nonlocal approach addresses early model failures and provides more stable results. The efficiency of the nonlocal scheme depends on the considered length scale controlled by the nonlocal parameters, γ^{nl} and ξ^{nl}. To study the influence of γ^{nl}, several analyses under $5mm\,s^{-1}$ loading rate for different values of γ^{nl} are performed when ξ^{nl} is maintained constant at $80\,kN$, and the results are extracted as force-displacement curves in Fig. 18. One can see that the effect of γ^{nl} is much smaller in its higher values. In other words, beyond

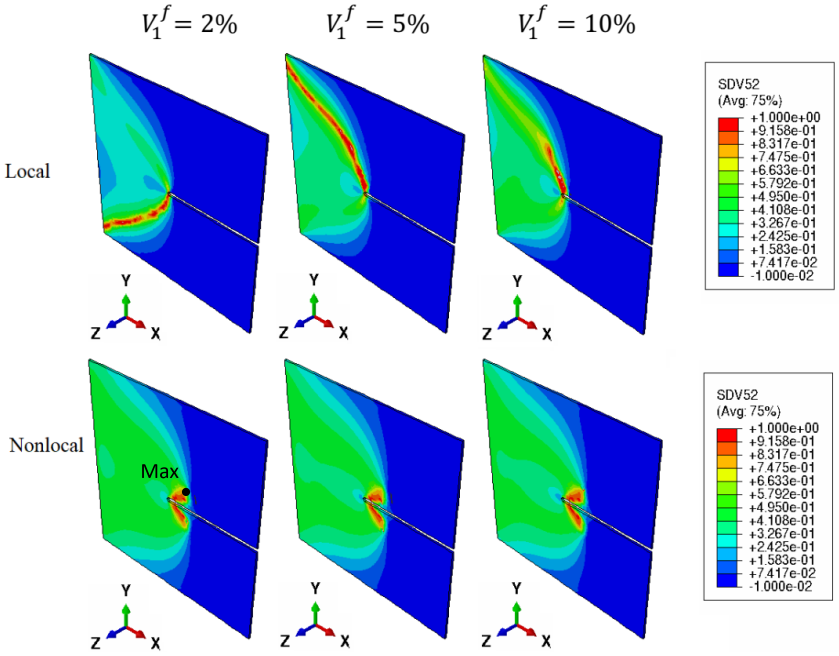

Figure 12: Matrix damage distribution in the notched plate under $5\,mm\,s^{-1}$ monotonic tensile loading using local and nonlocal models with $\xi^{nl} = 80\,\text{kN}$ and $\gamma^{nl} = 5\,\text{GPa}$ when $V_1^f = 2\%$, $V_1^f = 5\%$, and $V_1^f = 10\%$. The element type is the coupled temperature-displacement brick element (C3D8T).

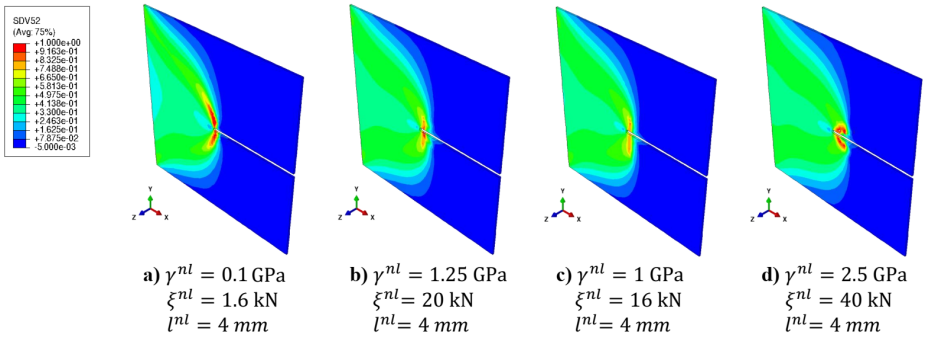

Figure 13: Matrix damage profile under $5\,mm\,s^{-1}$ monotonic tensile loading using the nonlocal model with different ξ^{nl} and γ^{nl} when the length scale is constant ($l^{nl} = 4\,mm$). The element type is the coupled temperature-displacement brick element (C3D8T).

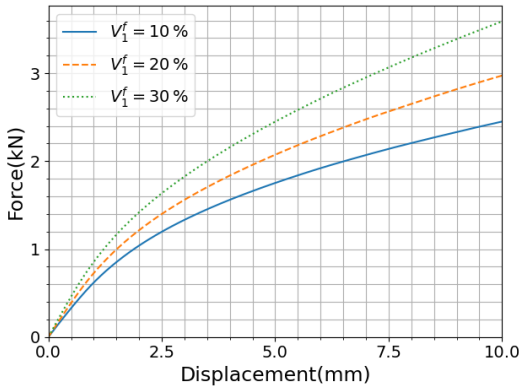

Figure 14: Force-displacement curves for the asymmetrically notched composite structure under $5\ mm\,s^{-1}$ monotonic loading rate in different glass volume fractions ($\gamma^{nl} = 5\,$GPa, $\xi^{nl} = 80\,$kN). The element type is the coupled temperature-displacement brick element (C3D8T).

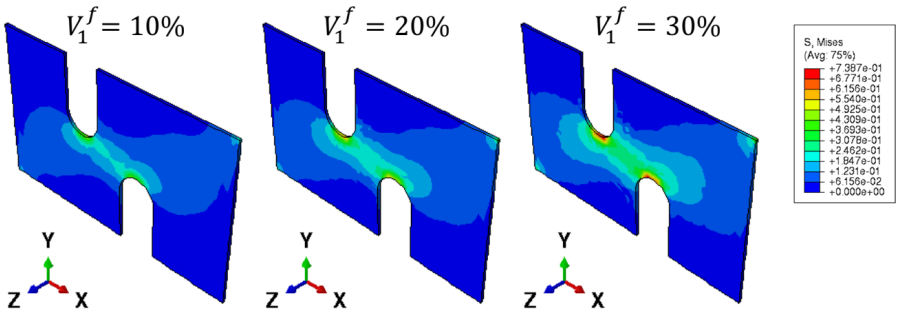

Figure 15: Von Mises stress distribution under 5 $mm\,s^{-1}$ monotonic loading rate for the asymetrically notched structure with $\gamma^{nl} = 5\,\text{GPa}$ and $\xi^{nl} = 80\,\text{kN}$ when $V_1^f = 10\%$, $V_1^f = 20\%$, and $V_1^f = 30\%$. The element type is the coupled temperature-displacement brick element (C3D8T). The results are extracted in the same time step (time= 2 s) and subsequently same displacement. It shows that the composite with higher glass volume fraction generates more stress concentration at the vicinity of the notches.

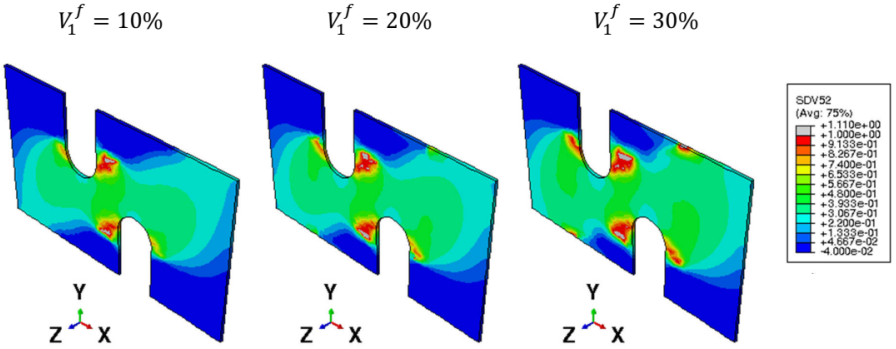

Figure 16: Damage profile under 5 $mm\,s^{-1}$ monotonic loading rate using the nonlocal model for the asymetrically notched structure with $\gamma^{nl} = 5\,\text{GPa}$ and $\xi^{nl} = 80\,\text{GPa}$ when $V_1^f = 10\%$, $V_1^f = 20\%$, $V_1^f = 30\%$. The element type is the coupled temperature-displacement brick element (C3D8T).

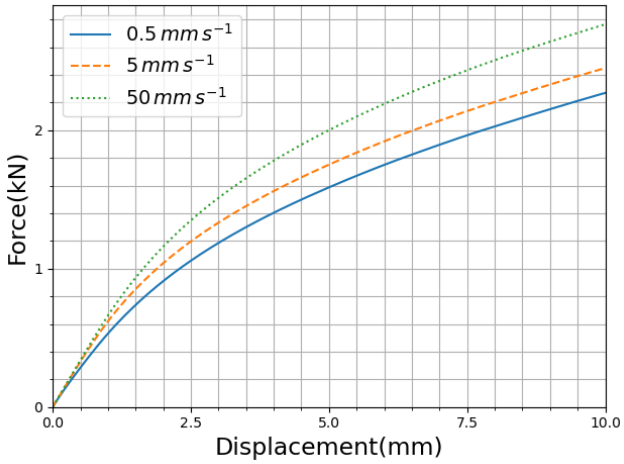

Figure 17: Force-displacement curves under different monotonic loading rates for the asymmetrically notched composite structure with $\gamma^{nl} = 5\,\text{GPa}$ and $\xi^{nl} = 80\,\text{kN}$ when $V_1^f = 10\%$. The element type is the coupled temperature-displacement brick element (C3D8T).

a certain level of γ^{nl}, the differences in the curves become negligible. Fig. 19 shows the effect of γ^{nl} in three different volume fractions, and as shown, its impact in all volume fractions is similar. By keeping $\gamma^{nl} = 5\,\text{GPa}$, the influence of ξ^{nl} is studied through several analyses under the same boundary conditions. Fig. 20 provides the force-displacement curves in several values of ξ^{nl} for three different volume fractions of glass fiber. As observed, for larger values of ξ^{nl} the model is stiffer and its impact does not change by increasing the glass fiber volume fraction. The softening zone and the sensitivity of the corresponding mesh have not been investigated in the present work. However, this has been discussed in detail in the previous research work (Satouri et al., 2022). From that study, for larger values of ξ^{nl}, the damaged zone evolves more widely around the crack zone, the mesh sensitivity is decreased, and the softening zone becomes smoother.

5. Conclusion and perspectives

In this study, the shortcoming of the conventional multi-scale models regarding the physical characterization of composites undergoing damage was addressed by a gradient enhanced nonlocal approach. In the microscale, the matrix phase constitutive laws have been derived using the ther-

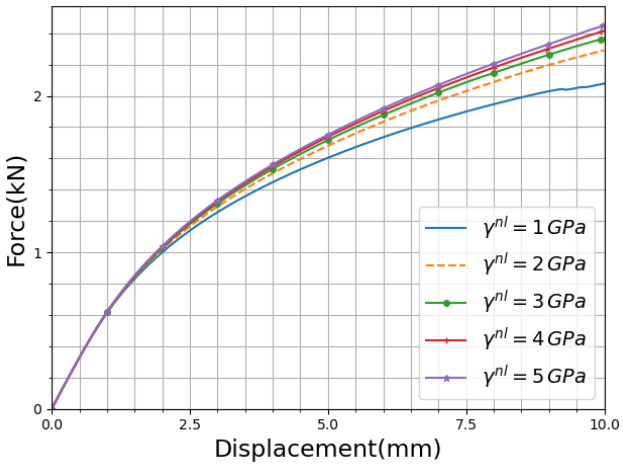

Figure 18: Force-displacement curves for the asymmetrically notched composite structure under 5 $mm\,s^{-1}$ loading rate in different γ^{nl} with $\xi^{nl} = 80\,kN$ when $V_1^f = 10\%$. The element type is the coupled temperature-displacement brick element (C3D8T).

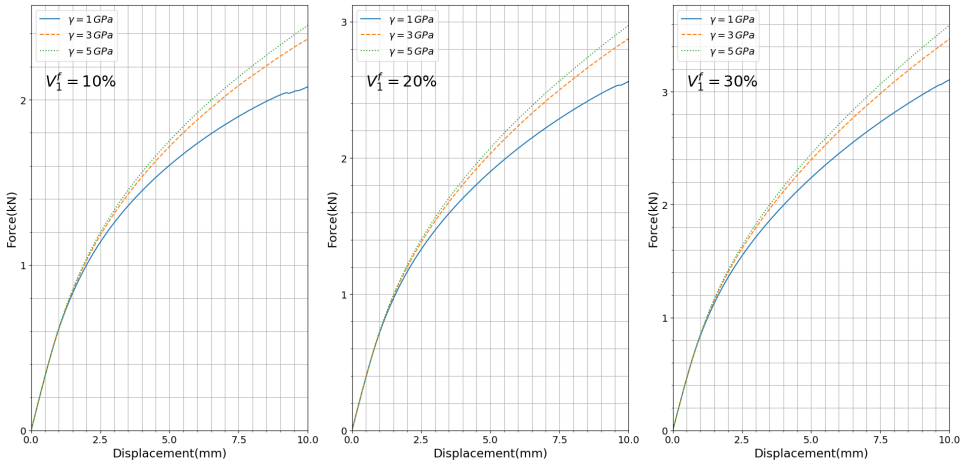

Figure 19: Force-displacement curves for the asymmetrically notched composite structure under 5 $mm\,s^{-1}$ monotonic loading rate in different γ^{nl} with $\xi^{nl} = 80\,kN$ when $V_1^f = 10\%$, $V_1^f = 20\%$, $V_1^f = 30\%$. The element type is the coupled temperature-displacement brick element (C3D8T).

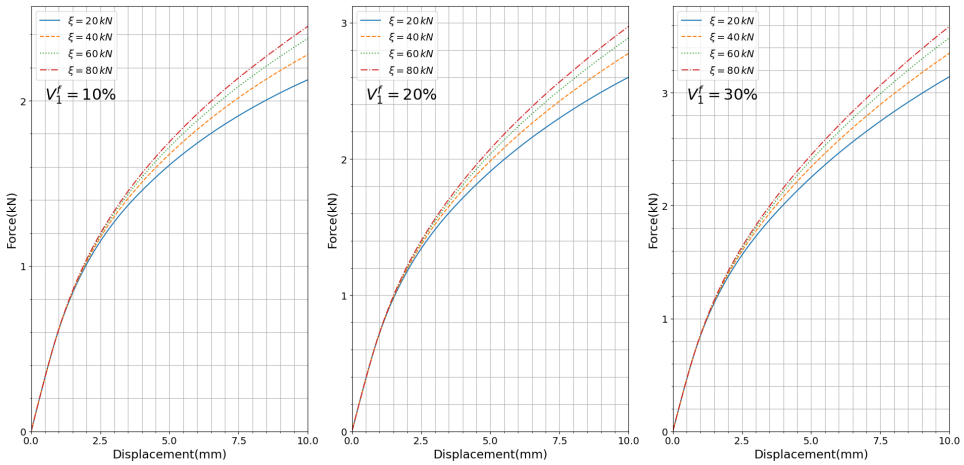

Figure 20: Force-displacement curves for the asymmetrically notched composite structure under 5 $mm\,s^{-1}$ monotonic loading rate in different ξ^{nl} with $\gamma^{nl} = 5\,\text{GPa}$ when $V_1^f = 10\%$, $V_1^f = 20\%$, $V_1^f = 30\%$. The element type is the coupled temperature-displacement brick element (C3D8T).

modynamics of irreversible processes and the generalized standard material formalism. To provide an appropriate multi-scale framework, the relationship between the nonlocal length scale and RVE size has been discussed, and the Mori-Tanaka/TFA approach has been suggested for homogenization when $l^{nl} \gg l^{\varepsilon}$, based on which the nonlocal approach is implemented at the macro scale. To develop the nonlocal field within the FE tool, an analogy between the steady state heat flux equation and the gradient enhanced relationship was considered, which allowed using the fully coupled temperature displacement package in ABAQUS. The numerical examples presented in this study express the capability of the nonlocal model to fully characterize material behaviors in high damage levels under small deformation assumption, and the resulting physical responses imply the good performance of the gradient enhanced thermodynamic model as a nonlocal approach in glass reinforced semi-crystalline polymers.

Temperature changes and relative humidity (RH), as environmental factors, have an undeniable impact on the material deformation and damage mechanisms in glass reinforced polymers (Arif et al., 2014b). Thus, to make the present model more comprehensive, it can be extended to a thermomechanical framework by including the effect of RH, the self-dissipation, and the corresponding thermomechanical coupling sources (Chatzigeorgiou et al., 2016; Benaarbia et al., 2019). Further-

more, to investigate polymeric composites mechanical behaviors more effectively, it is necessary to consider the effect of hydrostatic pressure and the asymmetry between compressive and tensile strength. Furthermore, since short glass fiber reinforced polyamide composites are more popular in the industry, extending the model, considering short fibers RVE, can provide further contribution to the multiscale analysis for different industrial applications. By accounting for these factors and calibrating the model using experimental data, the framework can be adopted to study real structures with engineering interest.

Appendix A. Asymptotic expansion

To investigate composites, material behaviors are expressed at two scales: micro and macro. The microscopic scale allows understanding the mechanisms considering the different material constituents and their geometrical characteristics in the microstructure. However, the macroscopic scale specifies the global response of the body as a homogeneous medium. The global volume of the body is considered as $\bar{V}$ on the spatial domain $\bar{\mathcal{B}}$ bounded by the surface $\partial\bar{\mathcal{B}}$ with unit vector $\bar{n}_i$. The microscale is defined through the unit cell volume,V within the spatial domain $\mathcal{B}$ bounded by the surface $\partial\mathcal{B}$ identified by the normal vector n_i. The micro and macro coordinate systems are respectively identified by x_i and $\bar{x}_i$ and related through the characteristic length, ε:

$$x_i = \bar{x}_i/\varepsilon. \tag{A.1}$$

The global composite coordinate system is expressed as x_i^ε, and the related derivatives are derived based on the chain rule:

$$\frac{\partial}{\partial x_i^\varepsilon} = \frac{\partial}{\partial \bar{x}_i} + \frac{1}{\varepsilon}\frac{\partial}{\partial x_i}. \tag{A.2}$$

Asymptotic expansion of the displacement vector, u_i^ε is defined as (Allaire, 1992; Bensoussan et al., 2011; Chatzigeorgiou et al., 2016):

$$u_i^\epsilon = u_i^{(0)}(\bar{x}_k, x_k) + \varepsilon u^{(1)}(\bar{x}_k, x_k) + \dots \tag{A.3}$$

Based on the small deformation theory, the strain and stress tensors are considered as:

$$\epsilon_{ij}^\varepsilon = \frac{1}{2}\left(\frac{\partial u_i^\varepsilon}{\partial x_j^\varepsilon} + \frac{\partial u_j^\varepsilon}{\partial x_i^\varepsilon}\right), \quad \sigma_{ij}^\varepsilon = C_{ijkl}^{sc}\epsilon_{kl}^\varepsilon. \tag{A.4}$$

Substituting (A.3) into (A.4) yields:

$$\begin{aligned}\epsilon_{ij}^{\varepsilon} =& \frac{1}{2}\left(\frac{\partial u_i^{(0)}}{\partial \bar{x}_j} + \varepsilon^{-1}\frac{\partial u_i^{(0)}}{\partial x_j} + \frac{\partial u_j^{(0)}}{\partial \bar{x}_i} + \varepsilon^{-1}\frac{\partial u_j^{(0)}}{\partial x_i}\right) \\ &+ \frac{1}{2}\varepsilon\left(\frac{\partial u_i^{(1)}}{\partial \bar{x}_j} + \varepsilon^{-1}\frac{\partial u_i^{(1)}}{\partial x_j} + \frac{\partial u_j^{(1)}}{\partial \bar{x}_i} + \varepsilon^{-1}\frac{\partial u_j^{(1)}}{\partial x_i}\right) + \ldots,\end{aligned} \tag{A.5}$$

where can be reduced as:

$$\epsilon_{ij}^{\varepsilon} = \varepsilon^{-1}\epsilon_{ij}^{(-1)}(\bar{x}_k, x_k) + \epsilon_{ij}^{(0)}(\bar{x}_k, x_k) + \varepsilon\epsilon_{ij}^{(1)}(\bar{x}_k, x_k) + \ldots, \tag{A.6}$$

with

$$\epsilon_{ij}^{(-1)} = \frac{1}{2}\left(\frac{\partial u_i^{(0)}}{\partial x_j} + \frac{\partial u_j^{(0)}}{\partial x_i}\right), \tag{A.7a}$$

$$\epsilon_{ij}^{(k)} = \frac{1}{2}\left(\frac{\partial u_i^{(k)}}{\partial \bar{x}_j} + \frac{\partial u_j^{(k)}}{\partial \bar{x}_i} + \frac{\partial u_i^{(k+1)}}{\partial x_j} + \frac{\partial u_j^{(k+1)}}{\partial x_i}\right), \quad k = 0, 1, 2, \ldots \tag{A.7b}$$

Using (A.4) and (A.6), the global stress tensor, $\boldsymbol{\sigma}^{\varepsilon}$, can be derived as:

$$\sigma_{ij}^{\varepsilon} = \varepsilon^{-1}C_{ijkl}^{sc}\epsilon_{kl}^{(-1)} + C_{ijkl}^{sc}\epsilon_{kl}^{(0)} + \varepsilon C_{ijkl}^{sc}\epsilon_{kl}^{(1)} + \ldots, \tag{A.8}$$

where can be reduced as:

$$\sigma_{ij}^{\varepsilon}(x_k^{\varepsilon}) = \varepsilon^{-1}\sigma_{ij}^{(-1)}(\bar{x}_k, x_k) + \sigma_{ij}^{(0)}(\bar{x}_k, x_k) + \varepsilon\sigma_{ij}^{(1)}(\bar{x}_k, x_k) + \ldots, \tag{A.9}$$

with

$$\sigma_{ij}^{(m)}(\bar{x}_k, x_k) = C_{ijkl}^{sc}\epsilon_{kl}^{(m)}, \quad m = -1, 0, 1, \ldots \tag{A.10}$$

The stress equilibrium in absence of the body forces in the global composite coordinate is given as:

$$\frac{\partial \sigma_{ij}^{\varepsilon}}{\partial x_j^{\varepsilon}} = 0. \tag{A.11}$$

Considering (A.2), it yields:

$$\frac{\partial \sigma_{ij}^{\varepsilon}}{\partial x_j^{\varepsilon}} = \frac{\partial \sigma_{ij}^{\varepsilon}}{\partial \bar{x}_j} + \frac{1}{\varepsilon}\frac{\partial \sigma_{ij}^{\varepsilon}}{\partial x_j}. \tag{A.12}$$

Substituting (A.10) into (A.12) results in:

$$\varepsilon^{-2}\frac{\partial\sigma_{ij}^{(-1)}}{\partial x_j}+\varepsilon^{-1}\frac{\partial\sigma_{ij}^{(-1)}}{\partial\bar{x}_j}+\varepsilon^{-1}\frac{\partial\sigma_{ij}^{(0)}}{\partial x_j}+\frac{\partial\sigma_{ij}^{(0)}}{\partial\bar{x}_j}+...=0. \tag{A.13}$$

The sum of the terms with the same power of ε can be taken as zero. For ε^{-2}, the following can be deduced:

$$\frac{\partial\sigma_{ij}^{(-1)}}{\partial x_j}=0. \tag{A.14}$$

Multiplying (A.14) in $u_i^{(0)}(x,\bar{x}_j)$ and integrating over the RVE yields:

$$\int_\Omega u_i^{(0)}(x_j,\bar{x}_j)\frac{\partial\sigma_{ij}^{(-1)}}{\partial x_j}dV=0. \tag{A.15}$$

Using the divergence theorem:

$$\int_{\partial\Omega}u_i^{(0)}(x_j,\bar{x}_j)\sigma_{ij}^{(-1)}n_jdS-\int_\Omega\frac{\partial u_i^{(0)}(x_j,\bar{x}_j)}{\partial x_j}\sigma_{ij}^{(-1)}dV=0. \tag{A.16}$$

Considering the anti-periodic term $\sigma_{ij}^{(-1)}n_j$ in (A.16), the surface integral is automatically zero, and the volume integral results in:

$$\frac{\partial u_i^{(0)}(x_j,\bar{x}_j)}{\partial x_j}=0. \tag{A.17}$$

It means that $u_i^{(0)}$ does not depend on the microscopic position vector, x_i. Accordingly asymptotic expansion of the displacement can be written as:

$$u_i^\epsilon(\bar{x}_k,x_k)=u_i^{(0)}(\bar{x}_k)+\epsilon u^{(1)}(\bar{x}_k,x_k)+\dots \tag{A.18}$$

In a similar way and using the nonlocal equation, (13), for the nonlocal variable, r^{nl}, the following asymptotic expansion can be derived:

$$r^{nl\varepsilon}(\bar{x}_k,x_k)=r^{nl(0)}(\bar{x}_k)+\varepsilon r^{nl(1)}(\bar{x}_k,x_k)+\varepsilon^2r^{nl(2)}(\bar{x}_k,x_k)+\dots \tag{A.19}$$

Accordingly, the asymptotic expansions can be written in summary as:

$$u_i^\epsilon(\bar{x}_k,x_k)=u_i^{(0)}(\bar{x}_k)+\varepsilon u^{(1)}(\bar{x}_k,x_k)+\dots, \tag{A.20a}$$

$$\epsilon_{ij}^{\varepsilon}(\bar{x}_k, x_k) = \epsilon_{ij}^{(0)}(\bar{x}_k, x_k) + \varepsilon\epsilon_{ij}^{(1)}(\bar{x}_k, x_k) + \dots, \tag{A.20b}$$

$$\sigma_{ij}^{\epsilon}(\bar{x}_k, x_k) = \sigma_{ij}^{(0)}(\bar{x}_k, x_k) + \varepsilon\sigma_{ij}^{(1)}(\bar{x}_k, x_k) + \dots, \tag{A.20c}$$

$$r^{\varepsilon}(\bar{x}_k, x_k) = r^{(0)}(\bar{x}_k, x_k) + \varepsilon r^{(1)}(\bar{x}_k, x_k) + \varepsilon^2 r^{(2)}(\bar{x}_k, x_k) + \dots, \tag{A.20d}$$

Appendix A.1. Stress equilibrium in the microscale

By substituting (A.20c) into the stress equilibrium in absence of the body forces, one obtains:

$$\frac{\partial \sigma_{ij}^{\varepsilon}}{\partial x_j^{\varepsilon}} = 0, \tag{A.21}$$

where is expanded as:

$$\frac{\partial}{\partial x_j^{\varepsilon}}\left(\sigma_{ij}^{(0)} + \varepsilon\sigma_{ij}^{(1)} + \dots\right) = 0. \tag{A.22}$$

Considering the chain rule, the above equation gives:

$$\frac{\partial \sigma_{ij}^{(0)}}{\partial \bar{x}_i} + \varepsilon^{-1}\frac{\sigma^{(0)}}{\partial x_i} + \varepsilon\left(\frac{\partial \sigma_{ij}^{(1)}}{\partial \bar{x}_i} + \varepsilon^{-1}\frac{\sigma_{ij}^{(1)}}{\partial x_i}\right) + \dots = 0. \tag{A.23}$$

Taking the terms with the same power of ε, it is rewritten as:

$$\varepsilon^{-1}\frac{\sigma_{ij}^{(0)}}{\partial x_i} + \left(\frac{\partial \sigma_{ij}^{(0)}}{\partial \bar{x}_i} + \frac{\sigma_{ij}^{(1)}}{\partial x_i}\right) + \varepsilon\left(\frac{\partial \sigma_{ij}^{(1)}}{\partial \bar{x}_i} + \frac{\sigma_{ij}^{(2)}}{\partial x_i}\right) + \dots = 0. \tag{A.24}$$

Considering the term multiplied by ε^{-1}, one obtains the following equation:

$$\frac{\sigma_{ij}^{(0)}}{\partial x_i} = 0. \tag{A.25}$$

Appendix A.2. Stress equilibrium in the macro scale

Averaging the term multiplied by ε^0 in (A.24) gives:

$$\langle\frac{\partial \sigma_{ij}^{(0)}}{\partial \bar{x}_i}\rangle + \langle\frac{\partial \sigma_{ij}^{(1)}}{\partial x_i}\rangle = 0, \tag{A.26}$$

where "$\langle.\rangle$" denotes the average operator defined as an integral over V:

$$\langle.\rangle = \frac{1}{V}\int_V .\, dV \tag{A.27}$$

Accordingly,(A.26) can be expanded as:

$$\frac{\partial\langle\sigma_{ij}^{(0)}\rangle}{\partial\bar{x}_i}+\frac{1}{V}\int_V\frac{\partial\sigma_{ij}^{(1)}}{\partial x_i}dV=0. \tag{A.28}$$

Using the divergence theorem, the above equation can be rewritten as following:

$$\frac{\partial\langle\sigma_{ij}^{(0)}\rangle}{\partial\bar{x}_i}+\frac{1}{V}\int_{\partial V}\sigma_{ij}^{(1)}n_j dS=0. \tag{A.29}$$

Due to the anti-periodicity of $\sigma_{ij}^{(1)}$, the second term in the (A.29) vanishes:

$$\frac{\partial\langle\sigma_{ij}^{(0)}\rangle}{\partial\bar{x}_i}=0, \tag{A.30}$$

or:

$$\frac{\partial\bar{\sigma}_{ij}}{\partial\bar{x}_i}=0\quad with\quad\langle\sigma_{ij}^{(0)}\rangle=\bar{\sigma}_{ij}. \tag{A.31}$$

Appendix A.3. Nonlocal equation in the microscale

Nonlocal equation in the global composite coordinate system is expressed as:

$$\xi^{nl}\frac{\partial}{\partial x_i^{\varepsilon}}\left(\frac{\partial r^{nl\varepsilon}}{\partial x_i^{\varepsilon}}\right)+\gamma^{nl}\left(r^{\varepsilon}-r^{nl\varepsilon}\right)=0 \tag{A.32}$$

The first derivative of the $r^{nl\varepsilon}$ can be defined as:

$$w_i^{nl\varepsilon}=\frac{\partial r^{nl\varepsilon}}{\partial x_i^{\varepsilon}}=\frac{\partial r^{nl\varepsilon}}{\partial\bar{x}_i}+\frac{1}{\varepsilon}\frac{\partial r^{nl\varepsilon}}{\partial x_i} \tag{A.33}$$

Substituting asymptotic expansion of $r^{nl\varepsilon}$ into (A.33) yields:

$$\begin{aligned}w_i^{nl\varepsilon}(\bar{x}_k,x_k)=&\frac{\partial}{\partial\bar{x}_i}\left(r^{nl(0)}(\bar{x}_k,x_k)+\varepsilon r^{nl(1)}(\bar{x}_k,x_k)+...\right)\\&+\frac{1}{\varepsilon}\frac{\partial}{\partial x_i}\left(r^{nl(0)}(\bar{x}_k,x_k)+\varepsilon r^{nl(1)}(\bar{x}_k,x_k)+...\right).\end{aligned} \tag{A.34}$$

where it is expanded to:

$$w_i^{nl\varepsilon}=\frac{\partial r^{nl(0)}}{\partial\bar{x}_i}+\varepsilon\frac{\partial r^{nl(1)}}{\partial\bar{x}_i}+...+\varepsilon^{-1}\frac{\partial r^{nl(0)}}{\partial x_i}+\frac{\partial r^{nl(1)}}{\partial x_i}+..., \tag{A.35}$$

where it can be rewritten as:

$$w_i^{nl\varepsilon}=\varepsilon^{-1}\frac{\partial r^{nl(0)}}{\partial x_i}+\left(\frac{\partial r^{nl(0)}}{\partial\bar{x}_i}+\frac{\partial r^{nl(1)}}{\partial x_i}\right)+\varepsilon\left(\frac{\partial r^{nl(1)}}{\partial\bar{x}_i}+\frac{\partial r^{nl(2)}}{\partial x_i}\right)+... \tag{A.36}$$

Accordingly, (A.33) can be reduced to its asymptotic expansion form as:

$$w_i^{nl\varepsilon} = \varepsilon^{-1} w_i^{nl(-1)} + w_i^{nl(0)} + \varepsilon w_i^{nl(1)} + ..., \tag{A.37}$$

with

$$w_i^{nl(-1)} = \frac{\partial r^{nl(0)}}{\partial x_i} = 0, \tag{A.38a}$$

$$w_i^{nl(0)} = \frac{\partial r^{nl(0)}}{\partial \bar{x}_i} + \frac{\partial r^{nl(1)}}{\partial x_i}, \tag{A.38b}$$

$$w_i^{nl(1)} = \frac{\partial r^{nl(1)}}{\partial \bar{x}_i} + \frac{\partial r^{nl(2)}}{\partial x_i}. \tag{A.38c}$$

Inserting (A.36) into (A.32) yields:

$$\xi^{nl} \frac{\partial w_i^{nl\varepsilon}}{\partial x_i^{\varepsilon}} + \gamma^{nl}(r^{(0)} - r^{nl(0)}) + \varepsilon\gamma^{nl}(r^{(1)} - r^{nl(1)}) + ... = 0, \tag{A.39}$$

where it is expanded as:

$$\xi^{nl}\left(\frac{\partial w_i^{nl\varepsilon}}{\partial \bar{x}_i} + \frac{1}{\varepsilon}\frac{\partial w_i^{nl\varepsilon}}{\partial x_i}\right) + \gamma^{nl}(r^{(0)} - r^{nl(0)}) + \varepsilon\gamma^{nl}(r^{(1)} - r^{nl(1)}) + ... = 0. \tag{A.40}$$

Substituting (A.37) into (A.40) yields:

$$\begin{aligned} &\xi^{nl}\left(\frac{\partial w_i^{nl(0)}}{\partial \bar{x}_i} + \varepsilon\frac{\partial w_i^{nl(1)}}{\partial \bar{x}_i} + ... + \varepsilon^{-2}\frac{\partial w_i^{nl(-1)}}{\partial x_i} + \varepsilon^{-1}\frac{\partial w_i^{nl(0)}}{\partial x_i} + \frac{\partial w_i^{nl(1)}}{\partial x_i} + ...\right) \\ &+ \gamma^{nl}(r^{(0)} - r^{nl(0)}) + \varepsilon\gamma^{nl}(r^{(1)} - r^{nl(1)}) + ... = 0. \end{aligned} \tag{A.41}$$

where it is reduced to:

$$\varepsilon^{-1}\xi^{nl}\frac{\partial w_i^{nl(0)}}{\partial x_i} + \left[\xi^{nl}\frac{\partial w_i^{nl(0)}}{\partial \bar{x}_i} + \xi^{nl}\frac{\partial w_i^{nl(1)}}{\partial x_i} + \gamma^{nl}\left(r^{(0)} - r^{nl(0)}\right)\right] + ... = 0. \tag{A.42}$$

The next sections discuss two probable cases concerning the relationship between the RVE size, l^{ε}, and the nonlocal length scale, l^{nl}: first, $l^{nl} \leq l^{\varepsilon}$ or l^{nl} comparable to l^{ε} , and second, $l^{nl} \gg l^{\varepsilon}$.

Appendix A.3.1. Nonlocal equation in the microscale in case 1: $l^{nl} \leq l^{\varepsilon}$ or l^{nl} comparable to l^{ε}

In this case, the length scale is less than or comparable to the RVE size. In other words, if $l^{\varepsilon} \to 0$ then $l^{nl} \to 0$, and the second term of (A.42) tends to become trivial when $l^{\varepsilon} \to 0$. Thus, the whole nonlocal equation (A.32) is present exclusively on the microscale and disappears from the macroscale. It has been shown in the literature that such case may cause issues on the homogenization framework (Fantoni et al., 2020).

Appendix A.3.2. Nonlocal equation for the microscale in case 2: $l^{nl} \gg l^{\varepsilon}$

In this case, it is assumed that $l^{nl} \gg l^{\varepsilon}$. With this in mind, the nonlocal variable, r^{nl}, stays uniform inside the RVE. Therefore,(A.42) is written as:

$$\frac{\partial w_i^{nl(0)}}{\partial x_i} = \frac{\partial}{\partial x_i}\left(\frac{\partial r^{nl(0)}}{\partial \bar{x}_i} + \frac{\partial r^{nl(1)}}{\partial x_i}\right) = 0. \tag{A.43}$$

(A.43) is the nonlocal equation in the microscale when $l^{nl} \gg l^{\varepsilon}$.

The first derivative of $r^{nl(1)}$ in the microscopic level can be assumed as:

$$\frac{\partial r^{nl(1)}}{\partial x_i} = \frac{\partial \mathcal{N}_j}{\partial x_i}\frac{\partial r^{nl(0)}}{\partial \bar{x}_j}. \tag{A.44}$$

Substituting (A.44) into (A.43) yields:

$$\frac{\partial}{\partial x_i}\left(\frac{\partial r^{nl(0)}}{\partial \bar{x}_j}\delta_{ij} + \frac{\partial \mathcal{N}_j}{\partial x_i}\frac{\partial r^{nl(0)}}{\partial \bar{x}_j}\right) = 0, \tag{A.45}$$

where it is reduced to:

$$\frac{\partial}{\partial x_i}\left(\delta_{ij} + \frac{\partial \mathcal{N}_j}{\partial x_i}\right) = 0. \tag{A.46}$$

where it means that $\partial N_j/\partial x_i$ is an arbitrary unknown constant, which can be taken zero. Hence, $w_i^{nl(0)}$ can be derived as:

$$w_i^{nl(0)} = \left(\delta_{ij} + \frac{\partial \mathcal{N}_j}{\partial x_i}\right)\frac{\partial r^{nl(0)}}{\partial \bar{x}_j} = \frac{\partial r^{nl(0)}}{\partial \bar{x}_i}, \tag{A.47}$$

where its average is obtained as:

$$\langle w_i^{nl(0)} \rangle = \frac{\partial r^{nl(0)}}{\partial \bar{x}_j}. \tag{A.48}$$

Appendix A.3.3. Nonlocal equation in the macroscale in case 2: $l^{nl} \gg l^{\varepsilon}$

Averaging the second term of (A.42) and considering $l^{\varepsilon} \to 0$, the macroscale equation is obtained as:

$$\langle \xi^{nl}\frac{\partial w_i^{nl(0)}}{\partial \bar{x}_i} + \xi^{nl}\frac{\partial w_i^{nl(1)}}{\partial x_i} + \gamma^{nl}(r^{(0)} - r^{nl(0)})\rangle = 0. \tag{A.49}$$

Considering the periodicity of $w_i^{nl(1)}$ in x_i, the second term vanishes:

$$\xi^{nl}\frac{\partial \langle w_i^{nl(0)}\rangle}{\partial \bar{x}_i} + \langle \gamma^{nl} r^{(0)}\rangle - \langle \gamma^{nl}\rangle r^{nl(0)} = 0. \tag{A.50}$$

Substituting (A.48) into (A.50) yields:

$$\xi^{nl}\frac{\partial}{\partial \bar{x}_i}\left(\frac{\partial r^{nl(0)}}{\partial \bar{x}_i}\right) + \langle \gamma^{nl} r^{(0)} \rangle - \langle \gamma^{nl} \rangle r^{nl(0)} = 0. \tag{A.51}$$

References

Aboudi, J. (2005). Micromechanically established constitutive equations for multiphase materials with viscoelastic–viscoplastic phases. *Mechanics of Time-Dependent Materials*, *9*, 121–145. doi:10.1007/s11043-005-1085-x.

Allaire, G. (1992). Homogenization and two-scale convergence. *SIAM Journal on Mathematical Analysis*, *23*, 1482–1518. doi:10.1137/0523084.

Arif, M., Saintier, N., Meraghni, F., Fitoussi, J., Chemisky, Y., & Robert, G. (2014a). Multiscale fatigue damage characterization in short glass fiber reinforced polyamide-66. *Composites Part B: Engineering*, *61*, 55–65. doi:10.1016/j.compositesb.2014.01.019.

Arif, M. F., Meraghni, F., Chemisky, Y., Despringre, N., & Robert, G. (2014b). In situ damage mechanisms investigation of pa66/gf30 composite: Effect of relative humidity. *Composites Part B: Engineering*, *58*, 487–495. doi:10.1016/j.compositesb.2013.11.001.

Arruda, E., & Boyce, M. (1993). A three-dimensional constitutive model for the large stretch behavior of rubber elastic materials. *Journal of The Mechanics and Physics of Solids*, *41*, 389–412. doi:10.1016/0022-5096(93)90013-6.

Bažant, Z., Belytschko, T., & Chang, T. (1984). Continuum theory for strain-softening. *Journal of Engineering Mechanics*, *110*, 1666–1692. doi:10.1061/(asce)0733-9399(1984)110:12(1666).

Barral, M., Chatzigeorgiou, G., Meraghni, F., & Léon, R. (2020). Homogenization using modified mori-tanaka and tfa framework for elastoplastic-viscoelastic-viscoplastic composites: theory and numerical validation. *International Journal of Plasticity*, *127*, 102632. doi:10.1016/j.ijplas.2019.11.011.

Benaarbia, A., Chatzigeorgiou, G., Kiefer, B., & Meraghni, F. (2019). A fully coupled thermo-viscoelastic-viscoplastic-damage framework to study the cyclic variability of the taylor-quinney coefficient for semi-crystalline polymers. *International Journal of Mechanical Sciences*, *163*, 105128. doi:10.1016/j.ijmecsci.2019.105128.

Benaarbia, A., Chrysochoos, A., & Robert, G. (2014). Influence of relative humidity and loading frequency on the pa6.6 cyclic thermomechanical behavior: part i. mechanical and thermal aspects. *Polymer Testing*, *40*, 290–298. doi:10.1016/j.polymertesting.2014.09.019.

Benaarbia, A., Chrysochoos, A., & Robert, G. (2016). Thermomechanical analysis of the onset of strain concentration zones in wet polyamide 6.6 subjected to cyclic loading. *Mechanics of Materials*, *99*, 9–25. doi:10.1016/j.mechmat.2016.04.011.

Bensoussan, A., Lions, J. L., Papanicolaou, G., & Caughey, T. (2011). Asymptotic analysis of periodic structures. *Journal of Applied Mechanics*, *46*, 477–477. doi:10.1115/1.3424588.

Benveniste, Y. (1987). A new approach to the application of mori-tanaka's theory in composite materials. *Mechanics of materials*, *6*, 147–157. doi:10.1016/0167-6636(87)90005-6.

Billon, N. (2012). New constitutive modeling for time-dependent mechanical behavior of polymers close to glass transition: Fundamentals and experimental validation. *Journal of Applied Polymer Science*, *125*, 4390–4401. doi:10.1002/app.36598.

Boyce, M., Parks, D., & Argon, A. (1988). Large inelastic deformation of glassy polymers. part i: rate dependent constitutive model. *Mechanics of Materials*, *7*, 15–33. doi:10.1016/0167-6636(88)90003-8.

Brunet, M., Morestin, F., & Walter-Leberre, H. (2005). Failure analysis of anisotropic sheet-metals using a non-local plastic damage model. *Journal of Materials Processing Technology*, *170*, 457–470. doi:10.1016/j.jmatprotec.2005.05.046.

Buckley, C., & Jones, D. (1995). Glass-rubber constitutive model for amorphous polymers near the glass transition. *Polymer*, *36*, 3301–3312. doi:10.1016/0032-3861(95)99429-x.

Castañeda, P. P. (1991). The effective mechanical properties of nonlinear isotropic composites. *J. Mech. Phys. Solids*, *39*, 45–e71. doi:10.1016/0022-5096(91)90030-R.

Chaboche, J. L. (1997). Thermodynamic formulation of constitutive equations and application to the viscoplasticity and viscoelasticity of metals and polymers. *International Journal of Solids and Structures*, *34*, 2239–2254. doi:10.1016/s0020-7683(96)00162-x.

Chatzigeorgiou, G. (2021). Study of multilayered composites through periodic homogenization and mori–tanaka methods. *Mechanics of Materials*, (p. 104110). doi:10.1016/j.mechmat.2021.104110.

Chatzigeorgiou, G., Benaarbia, A., & Meraghni, F. (2019). Piezoelectric-piezomagnetic behaviour of coated long fiber composites accounting for eigenfields. *Mechanics of Materials*, *138*, 103157. doi:10.1016/j.mechmat.2019.103157.

Chatzigeorgiou, G., Charalambakis, N., Chemisky, Y., & Meraghni, F. (2016). Periodic homogenization for fully coupled thermomechanical modeling of dissipative generalized standard materials. *International Journal of Plasticity*, *81*, 18–39. doi:10.1016/j.ijplas.2016.01.013.

Chatzigeorgiou, G., & Meraghni, F. (2019). Elastic and inelastic local strain fields in composites with coated fibers or particles: Theory and validation. *Mathematics and Mechanics of Solids*, *24*, 2858–2894. doi:10.1177/1081286518822695.

Chatzigeorgiou, G., Meraghni, F., & Charalambakis, N. (2022). *Multiscale Modeling Approaches for Composites*. Elsevier.

Chatzigeorgiou, G., Meraghni, F., Charalambakis, N., & Benaarbia, A. (2020). Multiscale modeling accounting for inelastic mechanisms of fuzzy fiber composites with straight or wavy carbon nanotubes. *International Journal of Solids and Structures*, *202*, 39–57. doi:10.1016/j.ijsolstr.2020.05.015.

Chen, Q., Chatzigeorgiou, G., & Meraghni, F. (2021). Extended mean-field homogenization of viscoelastic-viscoplastic polymer composites undergoing hybrid progressive degradation induced by interface debonding and matrix ductile damage. *International Journal of Solids and Structures*, *210*, 1–17. doi:10.1016/j.ijsolstr.2020.11.017.

Desrumaux, F., Meraghni, F., & Benzeggagh, M. L. (2001). Generalised mori-tanaka scheme to model anisotropic damage using numerical eshelby tensor. *Journal of Composite Materials*, *35*, 603–624. doi:10.1177/002199801772662091.

Dimitrijevic, B., & Hackl, K. (2011). A regularization framework for damage-plasticity models via gradient enhancement of the free energy. *International Journal for Numerical Methods in Biomedical Engineering*, *27*, 1199–1210. doi:10.1002/cnm.1350.

Doghri, I., & Ouaar, A. (2003). Homogenization of two-phase elasto-plastic composite materials and structures: Study of tangent operators, cyclic plasticity and numerical algorithms. *International Journal of Solids and structures*, *40*, 1681–1712. doi:10.1016/S0020-7683(03)00013-1.

Dvorak, G. J., & Benveniste, Y. (1992). On transformation strains and uniform fields in multiphase elastic media. *Proceedings of the Royal Society of London. Series A: Mathematical and Physical Sciences*, *437*, 291–310. doi:10.1098/rspa.1992.0062.

Fantoni, F., Bacigalupo, A., Paggi, M., & Reinoso, J. (2020). A phase field approach for damage propagation in periodic microstructured materials. *International Journal of Fracture*, *223*, 53–76. doi:10.1007/s42452-019-1890-5.

Forest, S. (2009). Nonlinear regularization operators as derived from the micromorphic approach to gradient elasticity, viscoplasticity and damage. *Proceedings of the Royal Society A: Mathematical, Physical and Engineering Sciences*, *472*, 20150755. doi:10.1098/rspa.2015.0755.

Fritzen, F., Forest, S., Böhlke, T., Kondo, D., & Kanit, T. (2012). Computational homogenization of elasto-plastic porous metals. *International Journal of Plasticity*, *29*, 102–119. doi:10.1016/j.ijplas.2011.08.005.

Geers, M., Borst, R., Brekelmans, W., & Peerlings, R. (1999). Validation and internal length scale determination for a gradient damage model: application to short glass-fibre-reinforced polypropylene. *International Journal of Solids and Structures*, *36*, 2557–2583. doi:10.1016/s0020-7683(98)00123-1.

Geers, M., Peerlings, R., Brekelmans, W., & De Borst, R. (2000). Phenomenological nonlocal approaches based on implicit gradient-enhanced damage. *Acta Mechanica*, *144*, 1–15. doi:10.1007/bf01181824.

Germain, P., Suquet, P., & Nguyen, Q. (1983). Continuum thermomechanics. *ASME Transactions Series E Journal of Applied Mechanics*, *50*, 1010–1020.

Govaert, L., Timmermans, P., & Brekelmans, W. (2000). The influence of intrinsic strain softening on strain localization in polycarbonate: modeling and experimental validation. *Journal of Engineering Materials and Technology*, *122*, 177–185. doi:10.1115/1.482784.

Halphen, B., & Nguyen, Q. (1975). On the generalized standards materials (in french). *Journal de Mécanique*, *14*, 39–63.

Hortig, C. (2010). *Local and non-local thermomechanical modeling and finite-element simulation of high-speed cutting*. Ph.D. thesis Dortmund, Techn. Univ., Diss., 2010.

Jirásek, M. (2002). Objective modeling of strain localization. *Revue Française de Génie Civil*, *6*, 1119–1132. doi:10.1080/12795119.2002.9692735.

Jirásek, M. (2007). Nonlocal damage mechanics. *Revue européenne de génie civil*, *11*, 993–1021. doi:10.3166/regc.11.993-1021.

Jirásek, M., Jirásek, M, Jirásek, M, Rolshoven, S., & Grassl, P. (1998). Nonlocal models for damage and fracture: Comparison of approaches. *International Journal for Numerical and Analytical Methods in Geomechanics*, *35*, 653–670. doi:10.1016/s0020-7683(97)00306-5.

Jirásek, M., Rolshoven, S., & Grassl, P. (2004). Size effect on fracture energy induced by nonlocality. *International Journal for Numerical and Analytical Methods in Geomechanics*, *28*, 653–670. doi:10.1002/nag.364.

Kiefer, B., Waffenschmidt, T., Sprave, L., & Menzel, A. (2018). A gradient-enhanced damage model coupled to plasticity—multi-surface formulation and algorithmic concepts. *International Journal of Damage Mechanics*, *27*, 253–295. doi:10.1177/1056789516676306.

Klompen, E., Engels, T., Govaert, L., & Meijer, H. (2005). Modeling of the postyield response of glassy polymers: influence of thermomechanical history. *Macromolecules*, *38*, 6997–7008. doi:10.1021/ma050498v.

Kotha, S., Ozturk, D., & Ghosh, S. (2019). Parametrically homogenized constitutive models (phcms) from micromechanical crystal plasticity fe simulations, part i: sensitivity analysis and parameter identification for titanium alloys. *International Journal of Plasticity*, *120*, 296–319. doi:10.1016/j.ijplas.2019.05.008.

Krairi, A., & Doghri, I. (2014). A thermodynamically-based constitutive model for thermoplastic polymers coupling viscoelasticity, viscoplasticity and ductile damage. *International Journal of Plasticity*, *60*, 163–181. doi:10.1016/j.ijplas.2014.04.010.

Kruch, S., & Chaboche, J.-L. (2011). Multi-scale analysis in elasto-viscoplasticity coupled with damage. *International Journal of Plasticity*, *27*, 2026–2039. doi:10.1016/j.ijplas.2011.03.007.

Lagoudas, D. C., Gavazzi, A. C., & Nigam, H. (1991). Elastoplastic behavior of metal matrix composites based on incremental plasticity and the mori-tanaka averaging scheme. *Computational Mechanics*, *8*, 193–203. doi:10.1007/bf00372689.

Lahellec, N., & Suquet, P. (2007). On the effective behavior of nonlinear inelastic composites: I. incremental variational principles. *Journal of the Mechanics and Physics of Solids*, *55*, 1932–1963. doi:10.1016/j.jmps.2007.02.003.

Launay, A., Maitournam, M., Marco, Y., Raoult, I., & Szmytka, F. (2011). Cyclic behaviour of short glass fibre reinforced polyamide: Experimental study and constitutive equations. *International Journal of Plasticity*, *27*, 1267–1293. doi:10.1016/j.ijplas.2011.02.005.

Love, B., & Batra, R. (2006). Determination of effective thermomechanical parameters of a mixture of two elastothermoviscoplastic constituents. *International Journal of Plasticity*, *22*, 1026–1061. doi:10.1016/j.ijplas.2005.07.001.

Mahnken, R., Schneidt, A., & Antretter, T. (2009). Macro modelling and homogenization for transformation induced plasticity of a low-alloy steel. *International Journal of Plasticity*, *25*, 183–204. doi:10.1016/j.ijplas.2008.03.005.

Mareau, C., Favier, V., Weber, B., Galtier, A., & Berveiller, M. (2012). Micromechanical modeling of the interactions between the microstructure and the dissipative deformation mechanisms in steels under cyclic loading. *International Journal of Plasticity*, *32-33*, 106–120. doi:10.1016/j.ijplas.2011.12.004.

Meraghni, F., Desrumaux, F., & Benzeggagh, M. (2002). Implementation of a constitutive micromechanical model for damage analysis in glass mat reinforced composite structures. *Composites Science and Technology*, *62*, 2087–2097. doi:10.1016/s0266-3538(02)00110-0.

Miehe, C., Aldakheel, F., & Raina, A. (2016). Phase field modeling of ductile fracture at finite strains: A variational gradient-extended plasticity-damage theory. *International Journal of Plasticity*, *84*, 1–32. doi:10.1016/j.ijplas.2016.04.011.

Miehe, C., Hofacker, M., & Welschinger, F. (2010). A phase field model for rate-independent crack propagation: Robust algorithmic implementation based on operator splits. *Computer Methods in Applied Mechanics and Engineering*, *199*, 2765–2778. doi:10.1016/j.cma.2010.04.011.

Mori, T., & Tanaka, K. (1973). Average stress in matrix and average elastic energy of materials with misfitting inclusions. *Acta metallurgica*, *21*, 571–574. doi:10.1016/0001-6160(73)90064-3.

Navidtehrani, Y., Betegón, C., & Martínez-Pañeda, E. (2021). A unified abaqus implementation of the phase field fracture method using only a user material subroutine. *Materials*, *14*, 1913. doi:10.3390/ma14081913.

Ostwald, R., Kuhl, E., & Menzel, A. (2019). On the implementation of finite deformation gradient-enhanced damage models. *Computational Mechanics*, *64*, 847–877. doi:10.1007/s00466-019-01684-5.

Paquet, D., Dondeti, P., & Ghosh, S. (2011). Dual-stage nested homogenization for rate-dependent anisotropic elasto-plasticity model of dendritic cast aluminum alloys. *International Journal of Plasticity*, *27*, 1677–1701. doi:10.1016/j.ijplas.2011.02.002.

Peerlings, R., Geers, M., Borst, D., & Brekelmans, W. (2001). A critical comparison of nonlocal and gradient-enhanced softening continua. *International Journal of Solids and Structures*, *38*, 7723–7746. doi:10.1016/s0020-7683(01)00087-7.

Pijaudier-Cabot, G., & Bažant, Z. P. (1987). Nonlocal damage theory. *Journal of engineering mechanics*, *113*, 1512–1533. doi:10.1061/(asce)0733-9399(1987)113:10(1512).

Praud, F., Chatzigeorgiou, G., Bikard, J., & Meraghni, F. (2017a). Phenomenological multi-mechanisms constitutive modelling for thermoplastic polymers, implicit implementation and experimental validation. *Mechanics of Materials*, *114*, 9–29. doi:10.1016/j.mechmat.2017.07.001.

Praud, F., Chatzigeorgiou, G., Chemisky, Y., & Meraghni, F. (2017b). Hybrid micromechanical-phenomenological modelling of anisotropic damage and anelasticity induced by micro-cracks in

unidirectional composites. *Composite Structures*, *182*, 223–236. doi:10.1016/j.compstruct.2017.09.013.

Praud, F., Chatzigeorgiou, G., & Meraghni, F. (2021a). Fully integrated multi-scale modelling of damage and time-dependency in thermoplastic-based woven composites. *International Journal of Damage Mechanics*, *30*, 163–195.

Praud, f., schmitt, t., zabeida, o., maïza, s., martinu, l., & lévesque, m. (2021b). Phase field fracture models to predict crack initiation and propagation in anti-reflective coatings. *Thin Solid Films*, *736*, 138920. doi:10.1016/j.tsf.2021.138920.

Qidwai, M., & Lagoudas, D. (2000). Numerical implementation of a shape memory alloy thermomechanical constitutive model using return mapping algorithms. *International Journal for Numerical Methods in Engineering*, *47*, 1123–1168. doi:10.1002/(sici)1097-0207(20000228)47:6<1123::aid-nme817>3.0.co;2-n.

Remond, Y. (2005). Constitutive modelling of viscoelastic unloading of short glass fibre-reinforced polyethylene. *Composites Science and Technology*, *65*, 421–428. doi:10.1016/j.compscitech.2004.09.010.

Satouri, S., Chatzigeorgiou, G., Benaarbia, A., & Meraghni, F. (2022). A gradient enhanced constitutive framework for the investigation of ductile damage localization within semicrystalline polymers. *International Journal of Damage Mechanics*, *31*, 1639–1675. doi:10.1177/10567895221115459.

Seupel, A., Hütter, G., & Kuna, M. (2018). An efficient fe-implementation of implicit gradient-enhanced damage models to simulate ductile failure. *Engineering Fracture Mechanics*, *199*, 41–60. doi:10.1016/j.engfracmech.2018.01.022.

Shutov, A., & Klyuchantsev, V. (2021). Large strain integral-based nonlocal simulation of ductile damage with application to mode-i fracture. *International Journal of Plasticity*, *144*, 103061. doi:10.1016/j.ijplas.2021.103061.

Silling, S. (2000). Reformulation of elasticity theory for discontinuities and long-range forces. *Journal of The Mechanics and Physics of Solids*, *48*, 175–209. doi:10.2172/1895.

Silling, S., & Lehoucq, R. (2010). Peridynamic theory of solid mechanics. In *Advances in Applied Mechanics* (pp. 73–168). Elsevier volume 44. doi:10.1016/s0065-2156(10)44002-8.

Simo, J. C., & Hughes, T. J. (2006). *Computational inelasticity* volume 7. Springer Science & Business Media.

Simone, A., Askes, H., & Sluys, L. (2004). Incorrect initiation and propagation of failure in non-local and gradient-enhanced media. *International Journal of Solids and Structures*, *41*, 351–363. doi:10.1016/j.ijsolstr.2003.09.020.

Suquet, P. (2012). Four exact relations for the effective relaxation function of linear viscoelastic composites. *Comptes Rendus Mécanique*, *340*, 387–399. doi:10.1016/j.crme.2012.02.022.

Terada, K., & Kikuchi, N. (2001). A class of general algorithms for multi-scale analyses of heterogeneous media. *Computer Methods in Applied Mechanics and Engineering*, *190*, 5427–5464. doi:10.1016/s0045-7825(01)00179-7.

Tervoort, T. A., Smit, R. J. M., Brekelmans, W. A. M., & Govaert, L. E. (1997). A constitutive equation for the elasto-viscoplastic deformation of glassy polymers. *Mechanics of Time-Dependent Materials*, *1*, 269–291.

Tikarrouchine, e., benaarbia, a., chatzigeorgiou, g., & meraghni, f. (2021). Non-linear fe2 multiscale simulation of damage, micro and macroscopic strains in polyamide 66-woven composite structures: analysis and experimental validation. *Composite Structures*, *255*, 112926. doi:10.1016/j.compstruct.2020.112926.

Tikarrouchine, E., Chatzigeorgiou, G., Praud, F., Piotrowski, B., Chemisky, Y., & Meraghni, F. (2018). Three-dimensional fe2 method for the simulation of non-linear, rate-dependent response of composite structures. *Composite Structures*, *193*, 165–179. doi:10.1016/j.compstruct.2018.03.072.

Wu, L., Noels, L., Adam, L., & Doghri, I. (2013). Non-local damage-enhanced mfh for multiscale simulations of composites. In *Composite Materials and Joining Technologies for Composites, Volume 7* (pp. 115–121). Springer New York. doi:10.1007/978-1-4614-4553-1_13.

Highlights:

1- Nonlocal multi-scale framework for composite materials accounting for viscoelasticity, viscoplasticity, and ductile damage.
2- Multi-scale analysis depending on the relation between RVE size and the nonlocal phenomena characteristic length.
3- Investigation of the localization phenomena at the macroscale taking into account the microstructure.
4- Combining for the first time mean-field homogenization technique and nonlocal ductile damage.
5- Validation of the framework against full scale analysis and parametric investigation of the nonlocal composite response.